The Astrophysical Journal, 974:37 (18pp), 2024 October 10 https://doi.org/10.3847/1538-4357/ad6b0c

Electrostatic Waves and Electron Holes in Simulations of Low-Mach Quasi-perpendicular Shocks

Artem Bohdan[1,2], Aaron Tran[3], Lorenzo Sironi[4], and Lynn B. Wilson, III[5]
[1] Max-Planck-Institut für Plasmaphysik, Boltzmannstr. 2, DE-85748 Garching, Germany
[2] Excellence Cluster ORIGINS, Boltzmannstr. 2, DE-85748 Garching, Germany
[3] Department of Physics, University of Wisconsin–Madison, 1150 University Ave, Madison, WI 53706, USA
[4] Department of Astronomy, Columbia University, 538 W 120th St. MC 5246, New York, NY 10027, USA
[5] Heliophysics Science Division, NASA Goddard Space Flight Center, Greenbelt, MD 20771, USA
Received 2024 June 5; revised 2024 July 30; accepted 2024 August 1; published 2024 October 3

Abstract

Collisionless low-Mach-number shocks are abundant in astrophysical and space plasma environments, exhibiting complex wave activity and wave–particle interactions. In this paper, we present 2D Particle-in-Cell (PIC) simulations of quasi-perpendicular nonrelativistic ($v_{\rm sh} \approx (5500–22000)\,{\rm km\,s^{-1}}$) low-Mach-number shocks, with a specific focus on studying electrostatic waves in the shock ramp and precursor regions. In these shocks, an ion-scale oblique whistler wave creates a configuration with two hot counterstreaming electron beams, which drive unstable electron acoustic waves (EAWs) that can turn into electrostatic solitary waves (ESWs) at the late stage of their evolution. By conducting simulations with periodic boundaries, we show that the EAW properties agree with linear dispersion analysis. The characteristics of ESWs in shock simulations, including their wavelength and amplitude, depend on the shock velocity. When extrapolated to shocks with realistic velocities ($v_{\rm sh} \approx 300\,{\rm km\,s^{-1}}$), the ESW wavelength is reduced to one-tenth of the electron skin depth and the ESW amplitude is anticipated to surpass that of the quasi-static electric field by more than a factor of 100. These theoretical predictions may explain a discrepancy, between PIC and satellite measurements, in the relative amplitude of high- and low-frequency electric field fluctuations.

Unified Astronomy Thesaurus concepts: Shocks (2086); Planetary bow shocks (1246); Space plasmas (1544); Plasma astrophysics (1261)

1. Introduction

Shock waves are ubiquitous, both in astrophysical environments and the solar system. They convert the bulk kinetic energy of supersonic plasma flows into the thermal energy of plasma and facilitate the production of high-energy particles, also known as cosmic rays. In most cases, the plasma involved can be treated as collisionless, therefore the energy exchange between plasma species inside the shock transition is governed by collective plasma behavior and wave–particle interaction. Earth's bow shock provides an excellent laboratory for studying these aspects of shock physics. Over the past 60 yr, it has been extensively investigated in situ by various satellite missions, such as Cluster (Horbury et al. 2001) and the Magnetospheric Multiscale (MMS) mission (Burch et al. 2016). These missions aim to study the microphysics of the Earth's magnetosphere, including the behavior of individual particles and fields at small scales, which is crucial for understanding fundamental processes such as magnetic reconnection, plasma turbulence, particle acceleration, etc.

The most recent mission, MMS, has made approximately 3000 passes through Earth's bow shock (Lalti et al. 2022). MMS has provided detailed measurements of electromagnetic fields, wave activity, plasma density, and high-energy particle distributions in the vicinity of the shock. However, satellite in situ measurements are limited to the spacecraft's trajectory, providing only a partial description of the shock's 3D structure. As a result, combining these measurements with kinetic plasma simulations can significantly enhance our understanding. Fully kinetic methods, such as Particle-in-Cell (PIC) simulations, have the capability to describe the evolution of shocks at ion scales and resolve the dynamics of electrons. Nevertheless, some discrepancies persist between kinetic simulations and in situ measurements. In this paper, we want to address the issue raised recently in Wilson et al. (2021)—namely, why in real shocks small-scale electrostatic fluctuations have much larger amplitude than quasi-static electric fields, in contrast to the findings of PIC simulations.

Electrostatic waves of different kinds are detected in situ near collisionless shocks. They include lower hybrid waves (Tidman & Krall 1971; Wu et al. 1984; Papadopoulos 1985; Walker et al. 2008), ion acoustic waves (IAWs; Fredricks et al. 1968, 1970; Gurnett & Anderson 1977; Kurth et al. 1979; Chen et al. 2018; Davis et al. 2021; Vasko et al. 2022), electrostatic solitary waves (ESWs) of both positive and negative polarity (Bale et al. 1998; Behlke et al. 2004; Wilson et al. 2007, 2010, 2014a; Goodrich et al. 2018; Malaspina et al. 2020; Wang et al. 2021), waves radiated by the electron cyclotron drift instability (Forslund et al. 1970; Lampe et al. 1972; Wilson et al. 2010), and Langmuir waves (Gurnett & Anderson 1977; Filbert & Kellogg 1979; Goodrich et al. 2018). For more details, see Wilson et al. (2021) and the citations therein. Some of them, e.g., IAWs and ESWs, are characterized by high frequencies and very short wavelengths (Wang et al. 2021; Vasko et al. 2022). Their typical amplitude $E \approx 100–200\,{\rm mV\,m^{-1}}$ is about 50–100 times higher than a typical convective (aka motional) electric field $\lesssim 4\,{\rm mV\,m^{-1}}$ measured in the satellite frame (Wilson et al. 2021, Figure 1).

Their wavelength is just a few tens of the Debye length or even smaller ($\lambda < 20\lambda_{De} \approx 0.1\lambda_{se} \approx 170$ m, where λ_{se} is the electron skin depth and λ_{De} is the electron Debye length).

In PIC simulations, we also can find a number of electrostatic instabilities. For instance, IAWs can be driven by the drift motion of preheated incoming ions relative to the decelerated electrons at the shock foot of high-Mach-number perpendicular shocks (Kato & Takabe 2010a, 2010b). Depending on the shock configuration, electron acoustic waves (EAWs) can be observed both in the shock foot, as a result of the modified two-stream instability (Matsukiyo & Scholer 2006), or in the upstream region of oblique shocks, where they are excited by high-energy electrons moving back upstream (Bohdan et al. 2022; Morris et al. 2022). Another example involves the excitation of electrostatic waves on the electron Bernstein mode branch by an ion beam (Dieckmann et al. 2000) when electron cyclotron drift instability becomes dominant. This excitation results in electrostatic waves at multiple electron cyclotron harmonic frequencies (Muschietti & Lembège 2006; Yu et al. 2022) within moderate-Mach-number perpendicular shocks. Furthermore, electrostatic Langmuir waves can be generated through the electron bump-on-tail instability (Sarkar et al. 2015) in the upstream region of oblique high-beta shocks (Kobzar et al. 2021). The Buneman instability (Buneman 1958) occurs between shock-reflected ions and cold upstream electrons, primarily at the shock foot of quasi-perpendicular high- (Shimada & Hoshino 2000; Hoshino & Shimada 2002; Amano & Hoshino 2007, 2009; Bohdan et al. 2017, 2019a, 2019b) and low- (Umeda et al. 2009) Mach-number shocks. In most of these PIC simulations, the wavelength of the electrostatic waves is comparable to the electron skin depth $\lambda \approx (1-5)\lambda_{se} \gg \lambda_{De}$ of the upstream plasma. Additionally, the amplitude of these waves at maximum is typically only a few times larger than the upstream motional electric field (E_0) appearing in simulations performed in the downstream rest reference frame, $E/E_0 \lesssim 2$, which appears inconsistent with satellite measurements. Note that for nonrelativistic shock simulations performed in the downstream plasma's rest frame, E_0 differs from the normal incidence frame motional electric field by a factor of $(1-1/r)$, where r is the density compression ratio. Following Wilson et al. (2021), we treat E_0 as comparable to spacecraft-frame measurements of the solar wind motional field within a factor of a few.

A potential explanation for the observed discrepancies between simulation results and in situ measurements lies in the choice of simulation parameters. In many cases, simulations adopt parameters that are unrealistic in order to ensure computational feasibility. Therefore, it is crucial to understand how the physical picture is distorted within simulations to accurately describe real systems. Depending on the problem in question, a range of correction techniques may be required for meaningful comparisons with in situ measurements. These can vary from minimal corrections, when magnetic field amplification by Weibel instability is considered (Bohdan et al. 2021), to more intricate rescaling calculations for problems of electron heating (Bohdan et al. 2020) or kinetic plasma waves (Verscharen et al. 2020), particularly when unrealistically high shock velocities or low ion-to-electron mass ratios are employed. In shock simulations, electrostatic waves can arise from various two-stream instabilities between drifting plasma components (ion–ion, ion–electron, or electron–electron). In such cases, the parameters of these waves could depend on the relative drift velocity between plasma components. Since the energy source of the relative plasma drift is the upstream plasma's bulk flow kinetic energy, the drift velocity could be roughly proportional to the shock velocity. Therefore, if a realistic shock velocity is utilized in a simulation, electrostatic waves may have different wavelengths and amplitudes than for typical PIC simulation parameters (unrealistically high shock velocities and low ion-to-electron mass ratios). Here, we aim to test this idea using PIC simulations and linear dispersion analysis.

The paper is structured as follows. Section 2 is dedicated to shock simulations. In Section 3, we discuss the results of the linear dispersion analysis and PIC simulations with periodic boundaries representing local regions within a shock. In Section 4, we discuss our results, and Section 5 summarizes our findings.

2. Shock Simulations

2.1. Simulation Setup

We use the PIC code TRISTAN-MP (Buneman 1993; Spitkovsky 2005) to simulate 2D quasi-perpendicular shocks with sonic Mach number $M_s = 4.0$, Alfvén Mach number $M_A = 1.8$, fast-mode Mach number $M_{fast} = 1.68$, upstream total plasma beta $\beta_p = 0.25$, and upstream magnetic field angle $\theta_{Bn} = 65°$ with respect to the shock-normal coordinate. The upstream magnetic field lies within the simulation plane. The same shock parameters (M_{fast}, β_p, θ_{Bn}) were studied by Tran & Sironi (2024, in their Section 7); here, we branch off of their work, using targeted 2D simulations to study electrostatic wave properties.

We form a shock by initializing a thermal plasma with bulk velocity $\boldsymbol{v}_0 = -v_0\hat{\boldsymbol{x}}$, single-species density n_0, and upstream temperature T_0. The plasma has two species: ions and electrons. The moving upstream plasma carries the magnetic field $\boldsymbol{B}_0$ and electric field $\boldsymbol{E}_0 = -\boldsymbol{v}_0 \times \boldsymbol{B}_0$, where $\boldsymbol{v}_0$ is the upstream plasma velocity in the simulation reference frame. The upstream plasma reflects on a conducting wall at $x = 0$, and the reflected plasma interacts with the upstream plasma to form a shock traveling toward $+\hat{\boldsymbol{x}}$. The simulation proceeds in approximately the downstream (i.e., post-shock) plasma's rest frame, except for a small drift in the shock-transverse direction that is expected for oblique shocks (Tidman & Krall 1971). The far x-boundary continuously expands toward $+\hat{\boldsymbol{x}}$ and injects fresh plasma into the simulation domain (Sironi & Spitkovsky 2009). The domain's y-boundaries are periodic.

The shock speed v_{sh}—i.e., the upstream flow speed in the shock's rest frame—is not directly chosen. We compute it as $v_{sh} = v_0/(1-1/r)$ in the nonrelativistic limit, with r being the density compression ratio estimated from the oblique magneto-hydrodynamic (MHD) Rankine–Hugoniot conditions assuming an adiabatic index $\Gamma = 5/3$ (Tidman & Krall 1971). By numerically inverting this procedure, we can choose v_0 to target a desired v_{sh} and hence Mach number. To relate v_{sh} and v_0 in Table 1, we use $r = 1.8496$. The targeted and actual Mach numbers agree to within ∼2%–7%. A more detailed explanation is given in Tran & Sironi (2024).

Standard plasma length scales and timescales are defined using upstream (pre-shock) plasma quantities; we use SI (MKS) units. The electron plasma frequency $\omega_{pe} = \sqrt{n_0 e^2/(\epsilon_0 m_e)}$, the electron cyclotron frequency $\Omega_e = eB_0/m_e$, the electron skin

Table 1
Shock Simulation Parameters

Run	m_i/m_e	v_{sh}/c	v_0/c	Width (λ_{si})	$\lambda_{De}/\lambda_{se} = v_{te0}/c$	ω_{pe}/Ω_e
A	200	0.0733	0.0338	2.90	0.143	1.76
B	200	0.0518	0.0238	2.71	0.100	2.49
C	200	0.0366	0.0168	2.90	0.071	3.52
D	200	0.0259	0.0119	2.71	0.050	4.99
E	200	0.0183	0.0084	2.90	0.036	7.05
B400	400	0.0367	0.0169	1.92	0.100	2.49
B800	800	0.0260	0.0119	1.36	0.100	2.49
B1836	1836	0.0171	0.0079	0.90	0.100	2.49

Note. All simulations have $M_s = 4$, $M_A = 1.8$, and $\theta_{Bn} = 65°$. The columns show the ion-to-electron mass ratio m_i/m_e, the shock velocity v_{sh}/c, the upstream velocity in the lab rest frame v_0/c, the simulation domain width L_y measured in terms of the ion skin depth λ_{si}, the ratio of upstream electron Debye and skin lengths $\lambda_{De}/\lambda_{se}$ (which equals v_{te0}/c), and the electron plasma-to-cyclotron frequency ratio ω_{pe}/Ω_e. To relate v_{sh} and v_0, we use $r = 1.8496$.

depth $\lambda_{se} = c/\omega_{pe}$, and the electron Debye length $\lambda_{De} = \sqrt{\epsilon_0 k_B T_0/(n_0 e^2)}$. Here, e is the elementary charge and ϵ_0 is the vacuum permittivity. The ion quantities ω_{pi}, λ_{si}, and Ω_i are defined analogously. We define the Mach numbers $M_s = v_{sh}/c_s$, $M_A = v_{sh}/v_A$, and $M_{fast} = v_{sh}/v_{fast}$. The shock speed v_{sh} is the upstream flow speed measured in the shock's rest frame, the sound speed $c_s = \sqrt{2\Gamma k_B T_0/(m_i + m_e)}$, the Alfvén speed $v_A = B_0/\sqrt{\mu_0 n_0 (m_i + m_e)}$, and the MHD fast speed $v_{fast} = \sqrt{0.5(c_s^2 + v_A^2 + \sqrt{(c_s^2 + v_A^2)^2 - 4c_s^2 v_A^2 \cos^2\theta_{Bn}})}$. The total plasma beta $\beta_p = 4\mu_0 n_0 k_B T_0/B_0^2$. The constants m_i and m_e are ion and electron masses, k_B is the Boltzmann constant, c is the speed of light, and μ_0 is the vacuum magnetic permeability. We define the initial electron rms thermal velocity $v_{te0} = \sqrt{k_B T_0/m_e}$.

Fixing the shock parameters (M_{fast}, β_p, θ_{Bn}), we vary v_{sh}/c and the ion–electron mass ratio m_i/m_e to study how the resulting shock structure depends upon the numerical compromises adopted for PIC simulations (Table 1). To vary v_{sh}/c, we rescale the dimensionless parameters v_0/c, $k_B T_0/(m_i c^2)$, and v_A/c, which are used to inject upstream plasma. If the flow and thermal speeds are nonrelativistic, we anticipate that the shock's macroscopic behavior may not depend on v_{sh}/c, or any other quantity scaled with respect to c (including ω_{pe}/Ω_e and ω_{pi}/Ω_i), so long as the dimensionless parameters M_s, β_p, θ_{Bn}, and m_i/m_e are fixed. Thus, PIC simulations with large $v_{sh} \sim 10^4$ km s^{-1} (and hence large T_0) may serve as analogs for natural systems with lower flow speeds $\sim 10^2$ km s^{-1}. In our simulations, all speeds are nonrelativistic, except for the electron thermal speed, which can be $\sim 0.1c$ (but the electron thermal energy remains $\ll m_e c^2$). However, electron-scale waves may be sensitive to v_{sh}/c (equivalently, ω_{pe}/Ω_e); these waves could in principle have a global effect upon shock structure. It is this subtler dependence that we seek to study.

All simulations have transverse width $L_y = 38.4\lambda_{se}$ (0.9 to $2.9\lambda_{si}$), duration $8.5\Omega_i^{-1}$, and spatial grid resolution $\Delta = 1.0\lambda_{De}$. The upstream plasma temperature $k_B T_0 = 10^{-4} m_i c^2$ for Run A and scales with $(v_{sh}/c)^2$ for other runs, so as to fix $M_s = 4$. The electron plasma-to-cyclotron frequency ratio $\omega_{pe}/\Omega_e = 1.8$–$7.0$ for Runs A–E, respectively. The runs of varying mass ratio (B, B400, B800, and B1836) all have $\omega_{pe}/\Omega_e = 2.49$. Note that for fixed β_p, ω_{pe}/Ω_e scales linearly with v_{sh}/c, and $\lambda_{De}/\lambda_{se}$ scales inversely with v_{sh}/c.

The runs in Table 1 use 128 particles per cell (64 per species), but we also perform variant simulations with up to 512 per cell (256 per species), to test convergence. We smooth the PIC current with 32 passes of a digital "1–2–1" filter on each coordinate axis, which imposes 50% power damping at wavenumber $k_{damp} \approx 0.25(\Delta)^{-1}$ (Birdsall & Langdon 1991, Appendix C).

2.2. Shock Properties

Figure 1 shows the structure of Run B at $t = 8.50\Omega_i^{-1}$, which exemplifies the general structure of all the simulations in Table 1. The shock speed v_{sh} is less than the phase speed of oblique whistlers traveling along the shock normal ($+\hat{\boldsymbol{x}}$), allowing a phase-standing precursor wave train to form ahead of the shock (Krasnoselskikh et al. 2002).

In Figure 1(a), the main $\boldsymbol{B}$-field compression (i.e., the shock ramp) takes place at $x \sim 8\lambda_{si}$, with compressive oscillations at larger x that gradually decay in the $+\hat{\boldsymbol{x}}$-direction. Figure 1(b) shows the shock-normal magnetic fluctuation $(B_x - B_{x0})/B_0$; recall that the upstream field component $B_{x0} \equiv B_0 \cos\theta_{Bn}$ is conserved across the shock jump. The B_x fluctuation reveals electromagnetic waves with $\boldsymbol{k}$ oriented oblique to both $\boldsymbol{B}_0$ and the shock normal (i.e., not phase-standing), which we call the oblique precursor. The oblique precursor has $\sim$100 time smaller amplitude than the $\hat{\boldsymbol{x}}$-aligned compressive waves in Figure 1(a). Both precursor wave trains in Figures 1(a) and (b) are right-hand-polarized, consistent with the fast-mode/whistler branch of the plasma dispersion relation.

The precursor wave trains at $t = 8.50\Omega_i^{-1}$ (Figure 1) are not in steady state. If the simulation proceeds to longer times $t \sim 40\Omega_i^{-1}$, then (i) the oblique precursor grows in amplitude, (ii) both the phase-standing and oblique precursors extend farther ahead of the shock, and (iii) density filamentation appears within and ahead of the shock ramp (Tran & Sironi 2024). We emphasize that our shock simulations are deliberately shorter in duration (not steady state) and also narrower in transverse width than some other fully kinetic PIC simulations in the recent literature (Xu et al. 2020; Lezhnin et al. 2021; Bohdan et al. 2022; Tran & Sironi 2024). The narrow transverse domain width $\sim 3\lambda_{si}$ helps preclude or slow the growth of other ion- and fluid-scale waves that would appear at shock-transverse scales of $\sim 10\lambda_{si}$ (Lowe & Burgess 2003; Burgess et al. 2016; Johlander et al. 2016; Trotta et al. 2023). The simulation parameters ensure that (i) the shock is steady on electron timescales, and (ii) its overall structure is dominated by a single, coherent precursor wave train without other ion-scale waves interfering. It aids our analysis to isolate

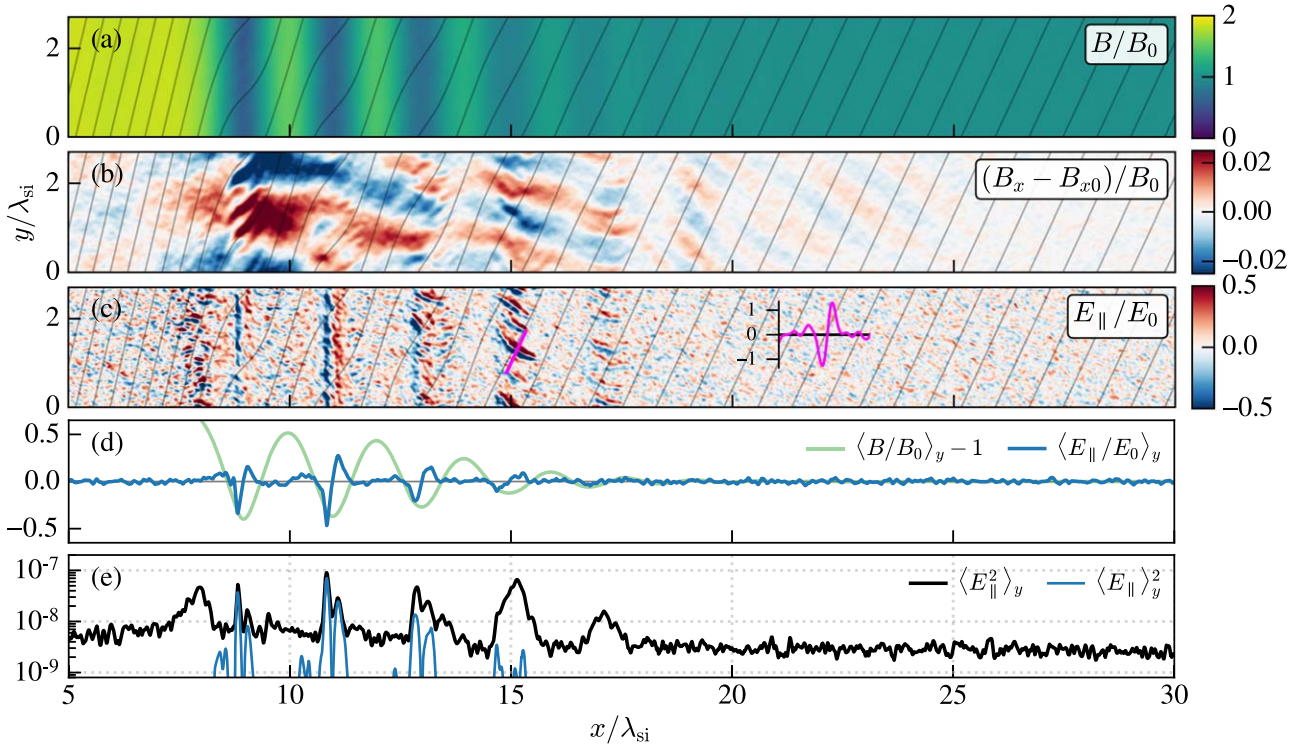

Figure 1. Overview of Run B at $t = 8.50\Omega_i^{-1}$. The shock travels from left to right and has its shock ramp at $x \approx 8\lambda_{si}$, which coincides with the largest density jump. (a) Magnetic field magnitude B/B_0. (b) Shock-normal magnetic fluctuation $(B_x - B_{x0})/B_0$, scaled to upstream field values B_0 and B_{x0}. (c) Parallel electric field, $E_\parallel/E_0$, measured with respect to local $\boldsymbol{B}$ and scaled to upstream motional electric field E_0. The inset waveform plot (magenta curve) shows the $E_\parallel/E_0$ waveform of a strong electron hole, measured along the magenta ray at $x = 15\lambda_{si}$. The abscissa increases along $\boldsymbol{B}$ and toward $+\hat{\boldsymbol{x}}$. (d) The y-averaged parallel electric field $\langle E_\parallel/E_0\rangle_y$ (blue) and magnetic fluctuation $\langle B/B_0\rangle_y - 1$ (green). (e) Total (black) and y-averaged (blue) parallel electric field energy densities in arbitrary units. In panels (a)–(c), the black contours trace magnetic field lines.

a single ion-scale wave mode that then forms ESWs; in real shocks, multiple ion-scale waves may exist in superposition to dictate the shock's behavior.

Figure 1(c) shows $E_\parallel \sim E_0$ fluctuations co-existing with the whistler precursor waves, where $E_0 = v_0 B_0$ is the magnitude of the upstream motional electric field. A laminar component with $\boldsymbol{k}\|+\hat{\boldsymbol{x}}$ appears at $x \sim 9$ to $13\lambda_{si}$, and smaller bipolar structures with $\boldsymbol{k}\|\boldsymbol{B}$ prevail at $x \sim 13$ to $18\lambda_{si}$. The bipolar structures have positive polarity: $E_\parallel$ points away from the center of the structure, so the electric potential $\phi(s) = -\int_{-\infty}^{s} E_\parallel(s')\mathrm{d}s'$ has local maximum at the structure's center, with s a magnetic-field-aligned coordinate. The typical 1D $E_\parallel$ profile of such a structure is shown as an inset (the magenta curve) in Figure 1(c). We refer to these electrostatic fluctuations as electron holes or ESWs (we use both names interchangeably), anticipating that they represent the nonlinear outcome of an electron–electron streaming instability to be shown in Section 3. The "hole" refers to a void in electron velocity space that forms within the self-consistent bipolar electrostatic fields (Hutchinson 2017).

Figure 1(d) shows the 1D y-averaged profiles $\langle E_\parallel\rangle_y$ and magnetic fluctuation $\langle B/B_0\rangle_y - 1$; we denote y-averaging by $\langle\cdots\rangle_y$. The $E_\parallel$ fluctuations near the shock with $\boldsymbol{k}\|+\hat{\boldsymbol{x}}$ form positive electrostatic potentials within the low-B parts of the precursor wave's cycle, which we call magnetic troughs. Figure 1(e) shows the total electrostatic parallel energy density $\langle E_\parallel^2\rangle_y$ (black). At $x \sim 9$ to $13\lambda_{si}$, we see that $\langle E_\parallel^2\rangle_y$ mostly arises from the y-averaged energy density $\langle E_\parallel\rangle_y^2$ (blue), which captures $E_\parallel$ fluctuations with $\boldsymbol{k}\|+\hat{\boldsymbol{x}}$. Left of the shock ramp, and right of $x \sim 13\lambda_{si}$, we see that $\langle E_\parallel^2\rangle_y$ arises from short-wavelength fluctuations not captured in $\langle E_\parallel\rangle_y^2$.

To show how the electron holes evolve in time, we track the real space trajectory of three example holes in Run B (Figure 2). To do so, we select the magnetic trough at $x \approx 14$ to $15\lambda_{si}$ and measure a 1D $E_\parallel(y)$ profile at an x-position offset $+\lambda/8$ from the magnetic trough's minimum (Figure 2, dashed black line), where λ is the local ion-scale precursor wavelength. Holes are identified as locations where $E_\parallel(y) = 0$ in between adjacent extrema $|E_\parallel|/E_0 > 0.33$. We track three manually chosen holes from $t = 8.0$ to $8.5\ \Omega_i^{-1}$. In the upstream plasma's rest frame, the hole velocities are $0.98v_{te0}$ (orange dot), $0.87v_{te0}$ (green dot), and $0.91v_{te0}$ (purple dot), recalling that v_{te0} is an upstream electron thermal velocity. By construction, all holes have upstream frame $v_x \approx v_{sh}$ within a few percent. The upstream frame $v_y = 3.0v_A$, $2.5v_A$, and $2.7v_A$ respectively; the velocity vectors have corresponding angles 59°, 54°, and 56° slightly below the local magnetic field angle of 62°–63°. The upstream frame velocity v is somewhat less than the Landau resonance velocity $\omega/k_\parallel \approx v_{sh}/\cos\theta_{Bn} = 1.22v_{te0}$.

In the Appendix, we present data from all of Runs A–E to establish that electron holes appear with amplitude exceeding the PIC noise and that both ω and $\boldsymbol{k}$ associated with the holes are well separated from other wave modes.

2.3. Electrostatic Energy Scaling with v_{sh}/c and m_i/m_e

How does the electrostatic energy density and wavenumber vary with v_{sh}/c? To compare these quantities between different simulations, we define four regions: the "Ramp," "Near

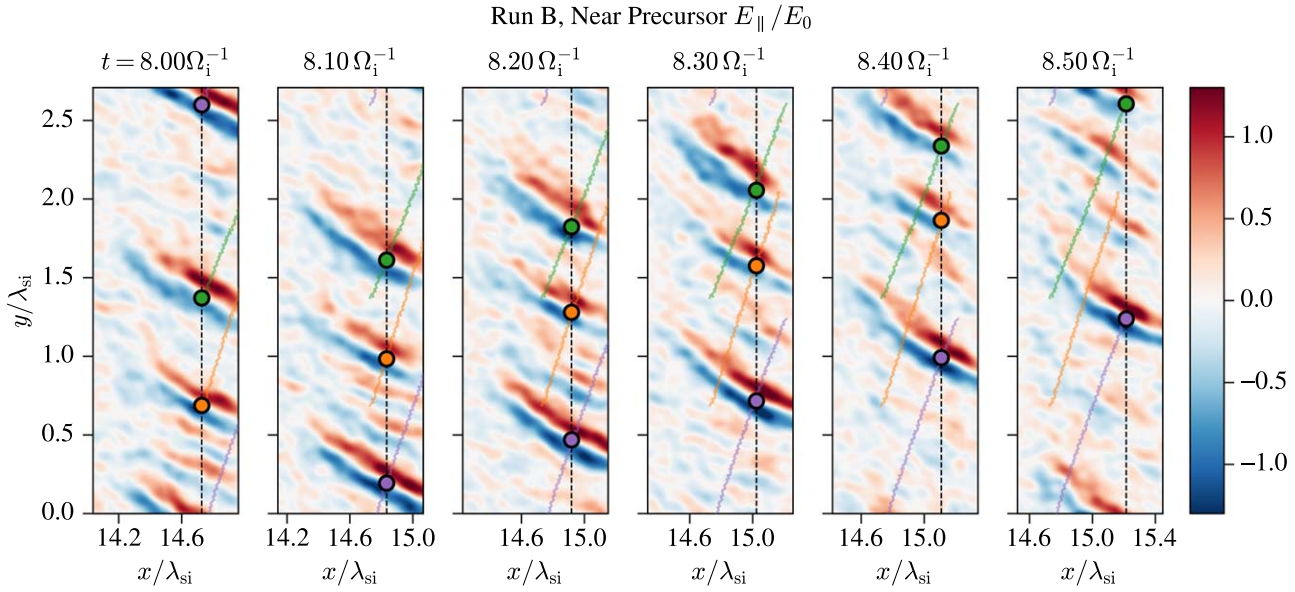

Figure 2. Three electron hole trajectories in Run B, tracked between 8.0 and 8.5 Ω_i^{-1}. The $E_\parallel/E_0$ panels advance in time from left to right, comoving with the shock's precursor wave train; the x- and y-axis coordinates are measured in the simulation frame. Individual electron holes are marked by the green, orange, and purple dots. The faint lines of corresponding color show their trajectories over time. The "Near Precursor" region shown is defined in Section 2.3.

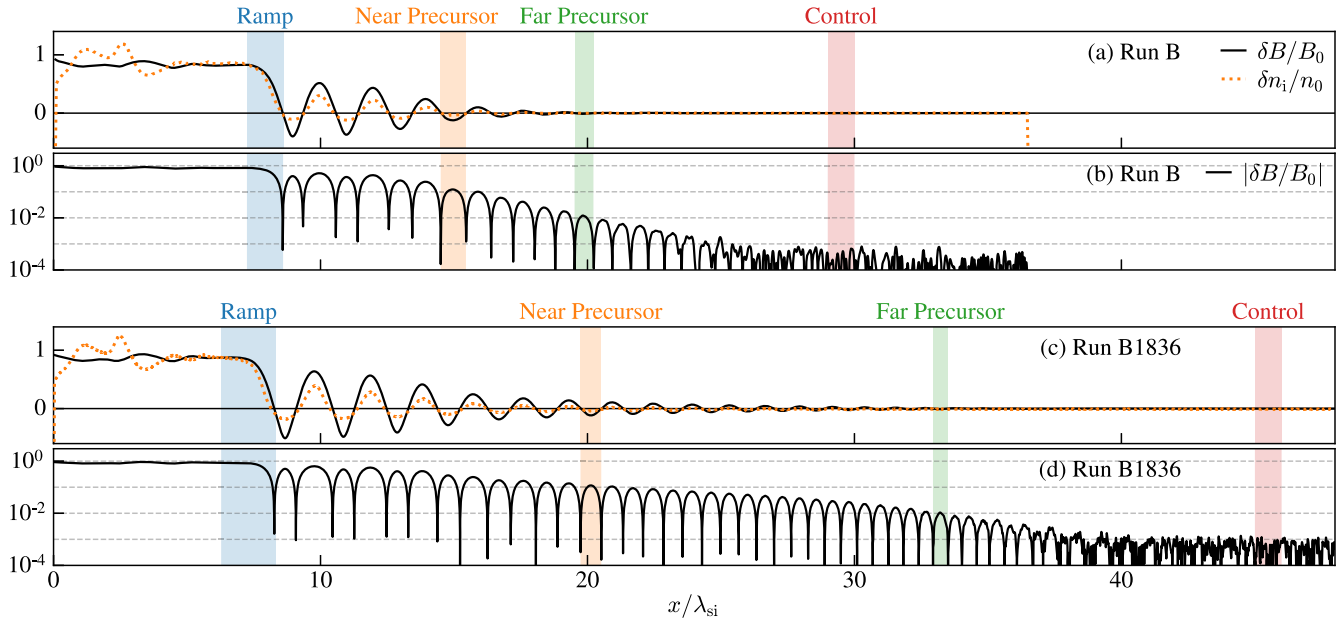

Figure 3. The electrostatic waves in Runs B and B1836 are measured in the colored regions: "Ramp" (blue), "Near Precursor" (orange), "Far Precursor" (green), and "Control" (red). In panels (a)–(b), the y-averaged fluctuations $\delta B/B_0$ (black) and $\delta n_i/n_0$ (orange dotted) show the region selection procedure for Run B. Panels (c)–(d) illustrate the same procedure for Run B1836. The "Near" and "Far Precursor" regions are magnetic troughs (wave half-cycles of low amplitude), with $|\delta B/B_0|$ just exceeding 0.1 and 0.01, respectively. The "Ramp" is the contiguous region where $\delta n_i/n_0 < \delta B/B_0$ (corresponding to $\delta B_{ff} > 0$) at the sharpest magnetic field increase in panels (a) and (c). The "Control" region samples undisturbed upstream plasma.

Precursor," "Far Precursor," and "Control," which are constructed as follows.

We segment the 1D, y-averaged, magnetic fluctuation strength $\delta B \equiv [B(x)/B_0] - 1$ by using its zero crossings to separate the precursor wave into half-cycles of low- and high-B amplitude, called troughs and crests, respectively (Figure 3(b)). Within the precursor, ESWs occur in troughs. The "Near Precursor" region is the rightmost segment with $\delta B < 0$ and extremum $|\delta B| \geqslant 0.1$ within the wave trough. The "Far Precursor" region is the rightmost segment with $\delta B < 0$ and extremum $|\delta B| \geqslant 0.01$ within the wave trough. For the precursor regions, dimensionless amplitude thresholds of 0.1 and 0.01 are chosen to select for nonlinear versus linear precursor wave behavior, respectively. For the "Ramp" region, we select an x-interval around the sharpest magnetic field increase, wherein magnetic flux freezing is locally broken such that the magnetic field is compressed more than the density, $\delta n_i/n_0 < \delta B/B_0$. Let $\delta B_{ff} \equiv [B(x)/B_{ff}(x)] - 1$, defining the flux-frozen field $B_{ff}(x) = B_0 n_i(x)/n_0$. We segment δB_{ff} using its zero crossings, and we select the unique region of $\delta B_{ff} > 0$ that

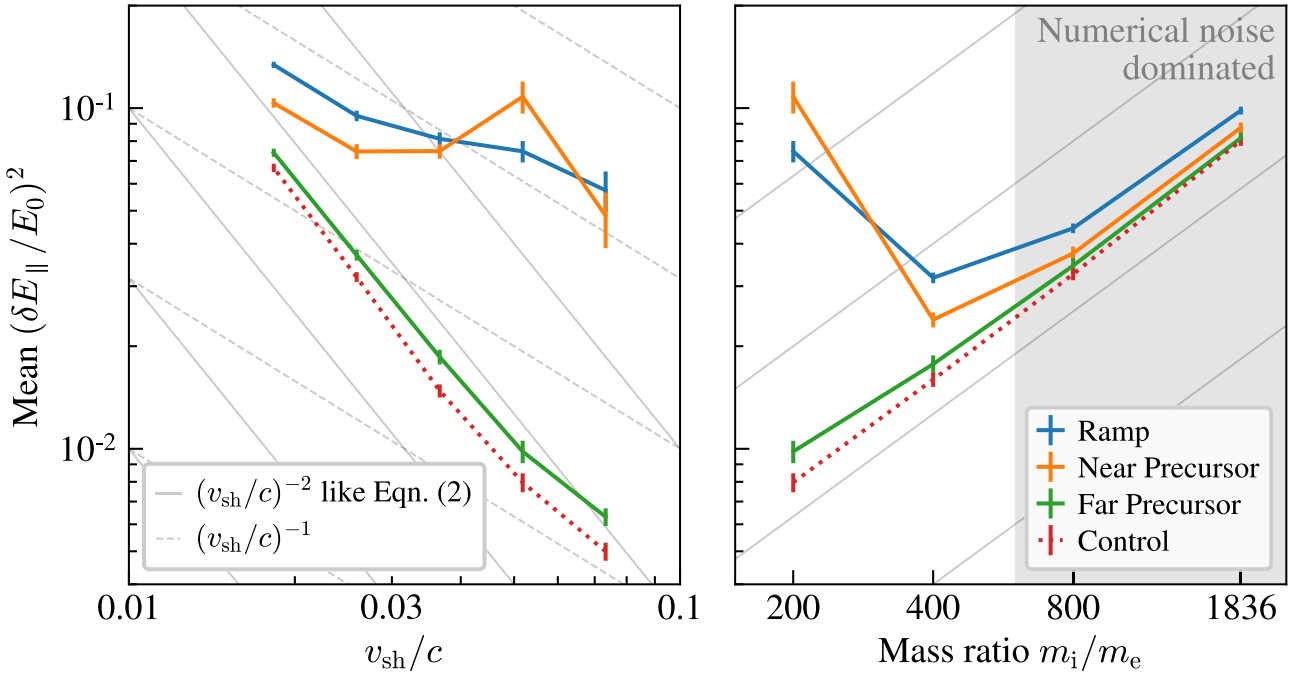

Figure 4. Left panel: scaling of the mean electrostatic energy density $\delta E_\parallel^2$ (Equation (1)) with v_{sh}/c, for four regions in each of Runs A–E. The solid gray lines show numerical noise scaling $(\delta E_\parallel/E_0)^2 \propto (v_{sh}/c)^{-2}$ like Equation (2); the dashed gray lines show $(\delta E_\parallel/E_0) \propto (v_{sh}/c)^{-1}$. Right panel: scaling with mass ratio m_i/m_e based on Runs B, B400, B800, and B1836. The solid gray lines show numerical noise scaling $(\delta E_\parallel/E_0)^2 \propto (v_{sh}/c)^{-2} \propto m_i/m_e$ appropriate for our simulation parameters. The electrostatic energy for Runs B800 and B1836 is dominated by numerical noise.

coincides with the conventionally defined shock ramp, i.e., the largest rise in magnetic field amplitude within the shock transition (Figures 3(a) and (c)). The so-chosen "Ramp" region has a similar width (1.1 to $1.4\lambda_{si}$) in all of Runs A–E. For higher-mass-ratio m_i/m_e, the precursor wave train extends for more cycles ahead of the shock. The region selections are thus spaced farther apart (Figures 3(c) and (d)). The "Control" region is fixed to the x-coordinate intervals 29–30, 35–36, 40–41, and 45–46 λ_{si} for Runs A–E, B400, B800, and B1836, respectively.

Figure 4 (left panel) shows how the electrostatic energy density $(\delta E_\parallel/E_0)^2$ scales with v_{sh}/c in each region. To improve the signal-to-noise ratio, we average $E_\parallel$ over (x, y, t) within the time interval $t = 8.00$ to $8.50\Omega_i^{-1}$. And we measure only fluctuations with wave vector $k_y \neq 0$ by subtracting the y-averaged contribution:

$$\delta E_\parallel^2 \equiv \langle E_\parallel^2 \rangle - \langle\langle E_\parallel \rangle_y^2 \rangle = \frac{1}{V} \iiint E_\parallel^2 \, dy \, dx \, dt - \frac{1}{V} \iint \left[\int E_\parallel \, dy \right]^2 dx \, dt, \quad (1)$$

where V is the 3D (x, y, t) integration volume, recalling from Figure 1 that the whistler precursor hosts $E_\parallel$ fluctuation with both k_y=0 and $k_y \neq 0$. For our chosen regions, $\langle E_\parallel^2 \rangle \gg \langle \langle E_\parallel \rangle_y^2 \rangle$. In Figure 4, the vertical error bars show the standard deviation, in time, of the space-averaged energy density in each region.

Both the "Far Precursor" and "Control" regions show $(\delta E_\parallel/E_0)^2 \propto (v_{sh}/c)^{-2}$ (Figure 4, left panel), which we attribute to numerical fluctuations. All of Runs A–E use the same number of PIC macroparticles per Debye sphere, Λ_p, so we expect $\delta E_\parallel^2 \propto n_e k_B T_e$ up to a constant prefactor that depends on Λ_p and the numerical particle shape (Section 5 of Melzani et al. 2013). Therefore,

$$\left(\frac{\delta E_\parallel}{E_0} \right)^2 \propto \beta_e (v_{sh}/c)^{-2}, \quad (2)$$

where β_e is the electron plasma beta.

In contrast, the "Ramp" and "Near Precursor" regions suggest a different scaling behavior, $(\delta E_\parallel/E_0)^2 \propto (v_{sh}/c)^0$ or $(v_{sh}/c)^{-1}$. The scaling may also show a turnover caused by a transition from mildly relativistic to nonrelativistic regimes, as thermal electrons attain velocities of $\sim$0.1 to $0.5c$ in Runs A and B, which have $v_{sh}/c = 0.0733$ and 0.0518, respectively.

The mass-ratio dependence is shown in the right panel of Figure 4. The energy density in the "Ramp" and "Near Precursor" regions decreases with the mass ratio m_i/m_e until reaching a numerical noise floor. For our simulations, the numerical noise $(\delta E_\parallel/E_0)^2 \propto (v_{sh}/c)^{-2} \propto (m_i/m_e)^1$ has an implicit mass-ratio scaling, because we hold v_{te0}/c constant while varying the mass ratio, which implies that $v_{sh}/c \propto (m_i/m_e)^{-1/2}$ in Equation (2).

Figure 5 checks whether the data in Figure 4 are converged with respect to numerical particle sampling. The energy density is mostly converged for $m_i/m_e = 200$ (Runs A–E), and it is nearly converged for $m_i/m_e = 400$ (Run B400). Higher mass ratios appear dominated by numerical noise.

2.4. Electrostatic Wavelengths

Let us now measure a characteristic electron hole wavenumber as a function of v_{sh}/c, using the Fourier power spectrum of $E_\parallel/E_0$ for the "Ramp" region. A Hann window function is applied along x and t to reduce power spectrum artifacts caused by the signal being aperiodic. We average the

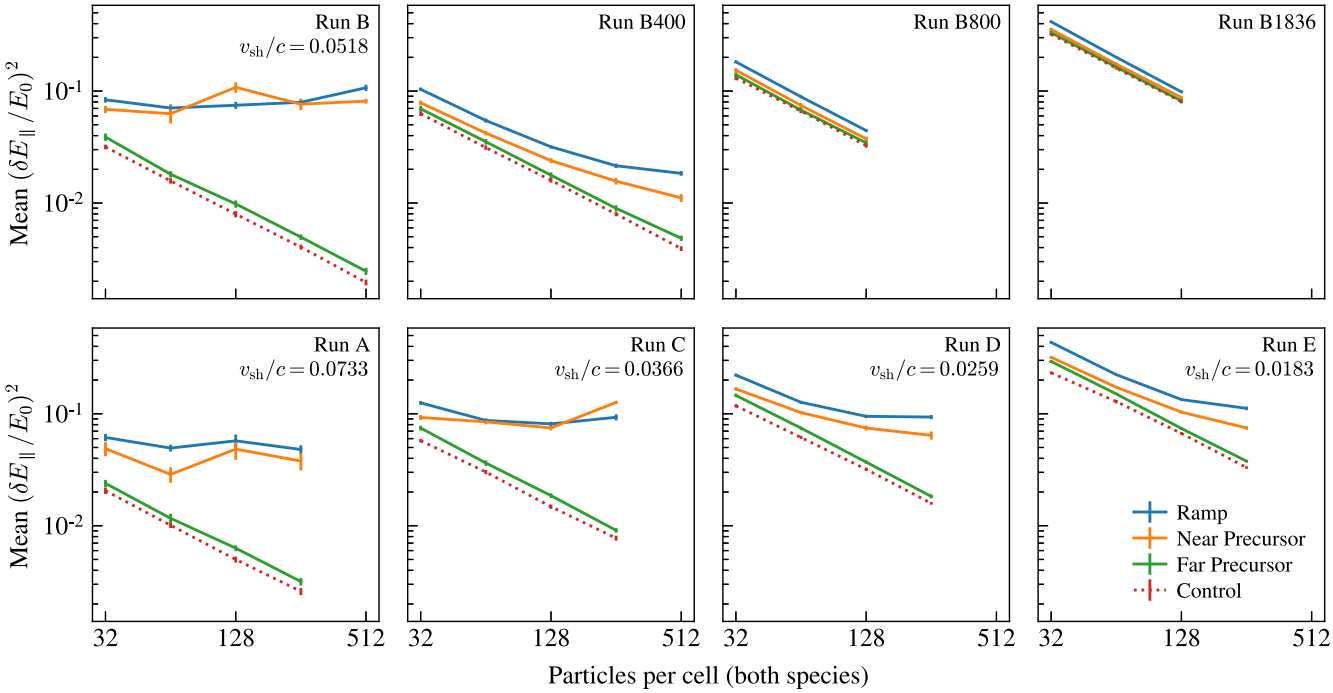

Figure 5. Like Figure 4, but showing numerical convergence with respect to the total number of particles per cell, counting both species. Runs A, B, and C are converged, based on the near-constant electrostatic energy density in the "Ramp" and "Near Precursor" regions; Runs D, E, and B400 are less or not converged. Runs B800 and B1836 are not converged and/or do not generate electrostatic fluctuations above numerical noise.

3D (k_x, k_y, ω) power spectrum over ω, and we then sample the 2D power spectrum in (k_x, k_y) by taking a ray along the local $\boldsymbol{B}$-field direction ($k_\perp = 0$) within each region. The resulting 1D spectrum is denoted $W(\boldsymbol{k})$ with vector argument to emphasize that the $k_\perp$ axis is not averaged.

Figure 6 shows $W(\boldsymbol{k})$ for the "Ramp" region of Runs A–E. The left column of Figure 6 scales $k_\parallel$ to the electron skin depth λ_{se}; the right column scales $k_\parallel$ to the electron Debye length λ_{De}. The thick translucent curve is the Fourier power spectrum of the upstream "Control" region, which shows the numerical noise floor for comparison. The vertical dashed line k_{damp} corresponds to a 50% damping imposed by the PIC current filtering described in Section 2.1. The vertical dotted line shows the peak wavenumber k_{max}, an ensemble-averaged wavenumber for all the wave power, defined as

$$k_{max} = \frac{\int k_\parallel W(\boldsymbol{k} = k_\parallel \hat{\boldsymbol{b}})\, dk_\parallel}{\int W(\boldsymbol{k} = k_\parallel \hat{\boldsymbol{b}})\, dk_\parallel}. \quad (3)$$

The electrostatic power resides at a fixed multiple of the electron Debye scale, not the skin depth. We further affirm this in Figure 7 by plotting $\lambda_{max} \equiv 2\pi/k_{max}$ as a function of v_{sh}/c, again normalized to either λ_{se} or λ_{De}, for the "Ramp" and "Near Precursor" regions. By eye, it is clear that $\lambda_{max}/\lambda_{se} \propto v_{sh}$, while $\lambda_{max}/\lambda_{De}$ does not depend on v_{sh}. Our measured λ_{max} can be reduced by a factor $1/\pi$ to compare to the hole length scales reported in satellite observations, which we discuss further in Section 4.2.

3. Electron Beam Model for EAW Driving

The shock simulations from the previous section demonstrate that electrostatic waves populate both the shock precursor and ramp regions. The amplitude of these waves scales as $(\delta E_\parallel/E_0)^2 \propto (v_{sh}/c)^{-1}$, while the wavelength scales as $\lambda_{max}/\lambda_{se} \propto v_{sh}$. In this section, we clarify the nature and properties of these electrostatic waves using linear dispersion analysis and PIC simulations with periodic boundaries.

We extract the electron momentum distributions from the "Ramp" and "Near Precursor" regions where electrostatic waves are present. Electron distributions from each sample region in Run B are illustrated in Figure 8. The distribution in the "Ramp" and "Near Precursor" regions of PIC simulated shocks consists of two hot streams of electrons, a pattern akin to the in situ observations made for Earth's bow shock (Feldman et al. 1982; Wilson et al. 2012). Notably, the measured in situ electron distributions can be modeled by a background Lorentzian distribution and a drifting Maxwellian beam. Early theoretical studies (Thomsen et al. 1983) demonstrated that such an electron distribution can drive EAWs if proper conditions are met. Using simulations of two electron beams with periodic boundaries, we check if the distributions extracted from PIC shock simulations are indeed able to drive EAWs, and we compare the results with numerical solutions of the hot-beams dispersion relation using the code WHAMP (Rönnmark 1982), which employs various approximations of the Fried–Conte plasma dispersion function.

3.1. Linear Dispersion Analysis

The distributions in Figure 8 can be represented with a bi-Gaussian distribution in the 1D case. After finding the best-fitting Gaussians, we see that the thermal velocities are 2 to 3 times smaller than the drift velocity ($v_{dr}/v_{th} \approx 2$–3), while the drift velocity is roughly 4 times larger than the shock velocity ($v_{dr}/v_{sh} \approx 4$) for simulations with $m_i/m_e = 200$ (runs A–E). Here, the drift velocity v_{dr} is calculated as the distance between the peaks of the two Gaussians and the thermal velocity v_{th} is the Gaussian's standard deviation, $v_{th} = \sqrt{k_B T_{e,\parallel}/m_e}$. We repeat this fitting procedure for all simulations in Table 1.

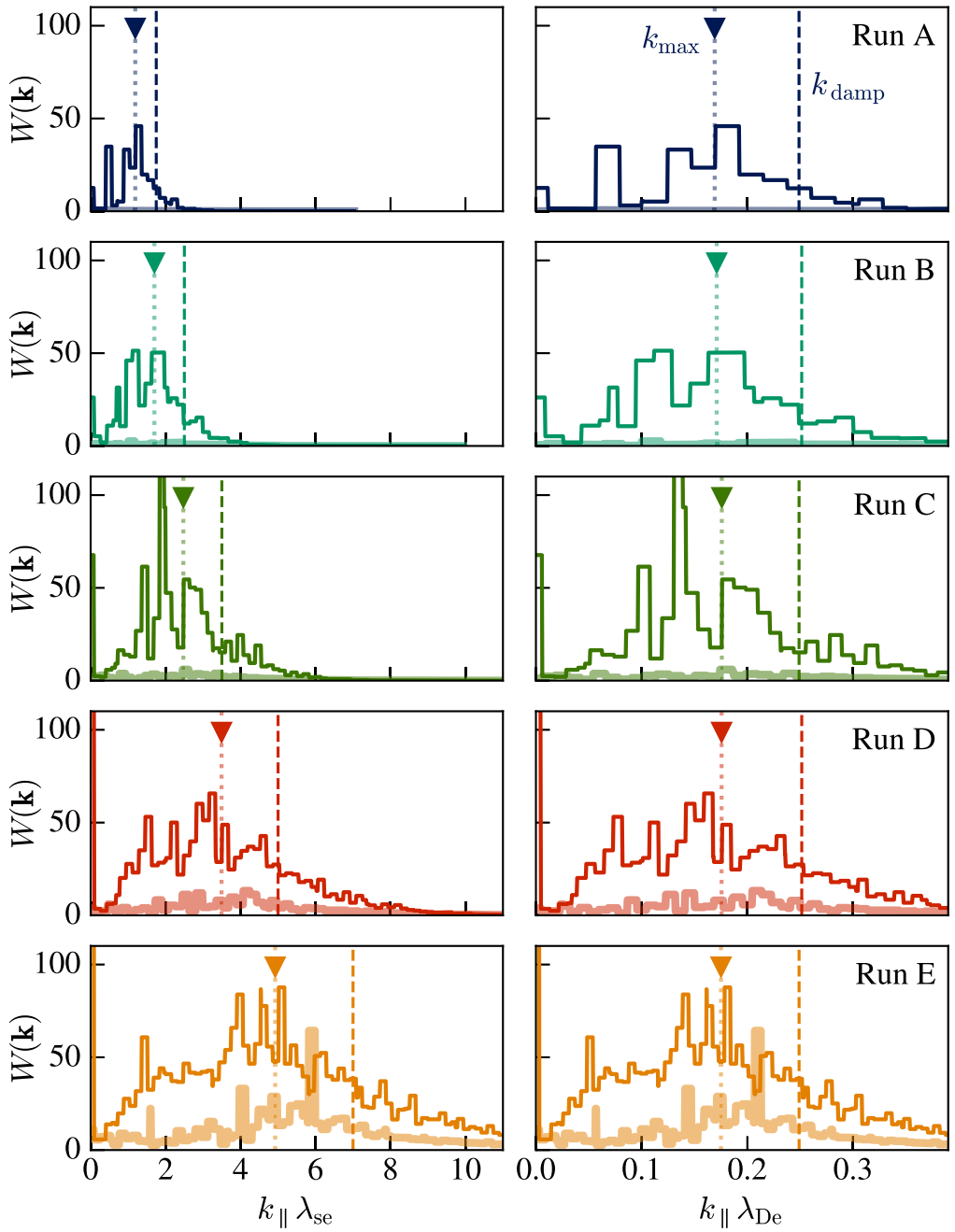

Figure 6. Electrostatic power spectrum $W(\boldsymbol{k} = k_\parallel \hat{\boldsymbol{b}})$, measured along the ray $k_\perp = 0$, for the "Ramp" region in Runs A–E. The left column shows $k_\parallel$ scaled to $\lambda_{\rm se}$; the right column shows $k_\parallel$ scaled to $\lambda_{\rm De}$. The thick translucent lines are the "Control" region power spectra. The triangle and dotted vertical line together mark $k_{\max}$ (Equation (3)). The dashed vertical line marks $k_{\rm damp}$, the damping wavelength set by the PIC current filtering.

The best-fit parameters of the electron distributions in the "Ramp" and "Near Precursor" regions for all simulations are summarized in Table 2. Since the normalized drift and thermal velocities do not depend on the shock velocity, we added a synthetic case (Run S), which is used to extrapolate a realistic shock scenario; it mimics a run with the average Earth bow-shock velocity of $v_{\rm sh} = 0.00104c = 312\,{\rm km\,s^{-1}}$ (Wilson et al. 2014b). The parameters of the electron beams (n_1/n_2, $v_{\rm dr}/v_{\rm sh}$, $v_{\rm dr}/v_{\rm th,1}$, and $v_{\rm dr}/v_{\rm th,2}$) for Run S were calculated as an average of the corresponding values from Runs A–E.

Figure 9 shows the growth rate of the EAWs calculated using WHAMP for both regions of interest for all shock simulations and the synthetic case. The growth rate of EAWs falls within the range of $\Gamma_{\max}/\omega_{\rm pe} \approx 0.01 - 0.04$ for the "Near Precursor" region and $\Gamma_{\max}/\omega_{\rm pe} \approx 0.05 - 0.08$ for the "Ramp" region. The frequency of EAWs is in range of $\omega/\omega_{\rm pe} = 0.3$–$0.4$ both for "Near Precursor" and "Ramp" regions. Note that the WHAMP calculations are done in the reference frame of the first beam, where it is stationary, and the second beam moves with $v = v_{\rm dr}$.

The growth rate shows slight variations across simulations (compare the growth rates for runs A–E), although the electron beam parameters are very similar. The growth rate is highly sensitive to $v_{\rm dr}/v_{\rm th}$ when hot beams are considered. For

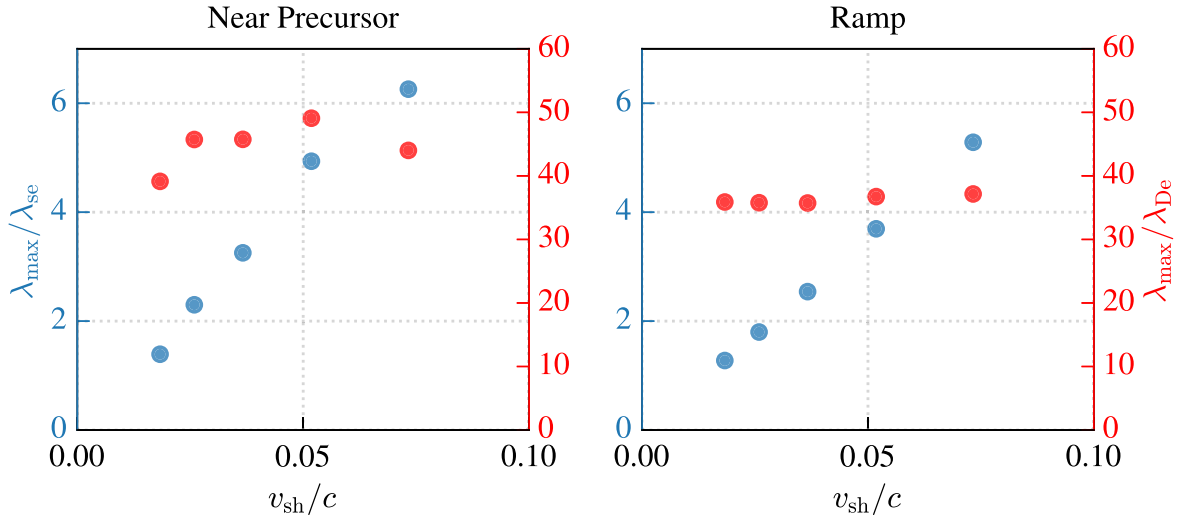

Figure 7. The electrostatic power spectrum's peak wavelength $\lambda_{max} \equiv 2\pi/k_{max}$ scaled to λ_{se} (blue dots) and λ_{De} (red dots) for the "Near Precursor" (left column) and "Ramp" (right column) regions.

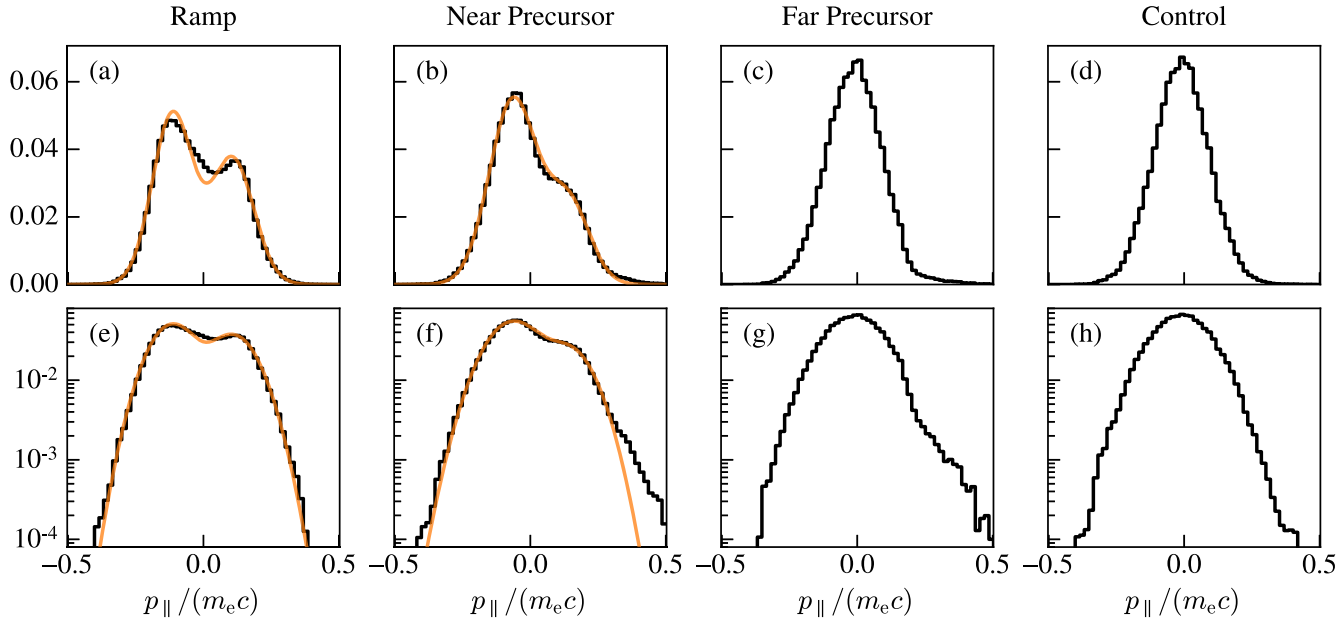

Figure 8. One-dimensional parallel momentum distribution, integrated over $p_\perp$, of electrons in the Run B shock regions (a) "Ramp," (b) "Near Precursor," (c) "Far Precursor," and (d) "Control." Panels (e)–(h) are the same, but with a logarithm-scaled y-axis. The black line is the average of many simulation snapshots ($t = 8.00$ to $8.50\Omega_i^{-1}$). The orange line is a best-fit bi-Gaussian distribution (Table 2).

example, $\Gamma_{max}/\omega_{pe} \approx 0.002$ for two beams with $v_{dr}/v_{th} = 2.3$, while the growth rate increases by an order of magnitude to $\Gamma_{max}/\omega_{pe} \approx 0.028$ when $v_{dr}/v_{th} = 2.5$. Nevertheless, shocks generally evolve on ion gyrotime scales, therefore

$$\Gamma/\Omega_i \approx (0.01 - 0.08) M_A (c/v_{sh}) \sqrt{m_i/m_e} \gg 1 \qquad (4)$$

indicates that EAWs reach a nonlinear stage in all shock simulations.

Consistent with the findings from shock simulations, the wavelength of the most unstable mode is proportional to the shock speed when normalized to the electron skin depth, $\lambda_{max}/\lambda_{se} \propto v_{sh}$, while it remains roughly constant when normalized to the Debye length, $\lambda_{max}/\lambda_{De} \approx$ const. However, the λ_{max} values predicted by WHAMP calculations are approximately half of those obtained from shock simulations (see Figure 9, bottom row). We address this discrepancy in the next subsection.

The parameters of the electron beams are influenced by the ion-to-electron mass ratio m_i/m_e (runs B, B400, B800, and B1836). As the mass ratio increases, the drift velocity also increases relative to v_{sh} as $v_{dr}/v_{sh} \propto \sqrt{m_i/m_e}$. However, the average value of the drift velocity relative to the thermal velocity of the drifting electrons decreases when the mass ratio increases. Consequently, the electron beams become too hot to excite EAWs, as evidenced by the reduced Γ_{max}/ω_{pe} values in Table 2.

3.2. Periodic-boundary-condition Simulations

In this section, we explore the evolution of EAWs using 2D periodic-boundary-condition simulations (PBCSs). For the initial momentum distribution of electrons, we adopt a

Table 2
Columns (2)–(5): Parameters of Electron Beams at "Near Precursor" and "Ramp" Regions for All Shock Simulations

1	2	3	4	5	6	7	8	9	10
Run	$\frac{n_1}{n_2}$	$\frac{v_{dr}}{v_{sh}}$	$\frac{v_{dr}}{v_{th,1}}$	$\frac{v_{dr}}{v_{th,2}}$	$\frac{\lambda_{max}}{\lambda_{se}}$	$\frac{\lambda_{max}}{\lambda_{De}}$	$\frac{\Gamma_{max}}{\omega_{pe}}$	$\left(\frac{\lambda_{max}}{\lambda_{se}}\right)_{sh}$	$\left(\frac{\lambda_{max}}{\lambda_{De}}\right)_{sh}$
Near Precursor									
A	2.35	3.89	2.35	2.69	4.49	31.6	0.013	6.26	44.0
B	2.22	3.91	2.34	2.68	3.13	31.1	0.013	4.94	49.1
C	2.25	3.87	2.33	2.92	1.82	25.6	0.029	3.25	45.8
D	2.10	3.86	2.29	3.12	1.10	21.8	0.041	2.30	45.7
E	1.93	3.84	2.32	3.04	0.76	21.8	0.043	1.39	39.1
S	2.17	3.87	2.33	2.89	0.052	26.0	0.025		
Ramp									
A	1.52	4.14	2.79	2.78	2.74	19.3	0.057	5.28	37.2
B	1.36	4.15	2.88	2.75	1.58	15.8	0.076	3.69	36.7
C	1.33	4.16	2.96	2.61	1.36	19.2	0.060	2.54	35.7
D	1.28	4.19	2.99	2.45	1.03	20.5	0.050	1.80	35.8
E	1.26	4.28	3.02	2.40	0.76	21.5	0.050	1.28	35.9
S	1.35	4.19	2.93	2.59	0.04	20.1	0.049	⋯	⋯
B400	1.02	5.15	2.69	2.17	2.89	28.9	0.019	⋯	⋯
B800	0.86	6.89	2.55	1.99	10.2	102	0.00041	⋯	⋯
B1836	0.66	10.2	2.42	1.76	⋯	⋯	stable	⋯	⋯

Notes. Columns (2)–(5): parameters of electron beams at the "Near Precursor" and "Ramp" regions for all shock simulations. The subscript "1" corresponds to the denser electron beam moving against the magnetic field, and the subscript "2" corresponds to the diluted electron beam moving along the magnetic field. Run S is a synthetic run with a realistic shock velocity of $v_{sh} = 312$ km s^{-1} (Wilson et al. 2014b). Columns (6)–(8): parameters of the most unstable electron acoustic mode, according to the linear dispersion analysis. Columns (9)–(10): peak wavelength of the electrostatic power spectrum in shock simulations.

bi-Gaussian distribution to represent two hot counterstreaming beams. We initialize two equal-density beams with $v_{dr}/v_{th,1} = 3$ and $v_{dr}/v_{th,2} = 5$. These drift speeds exceed the shock-based measurements in Table 2, because we suppose that the electron beams in a shock represent the steady-state outcome of initially unstable conditions, which may be modeled as having a larger initial beam drift. The beams move in opposite directions with magnitudes $|v_1| = |v_2| = v_{dr}/2$. To comprehensively study the behavior of EAWs, we conduct multiple simulations, varying parameters such as v_{dr}, spatial and temporal resolutions, ion presence/absence and mass ($m_i/m_e = 200$ and 1836), and the number of particles per cell; we keep $v_{dr}/v_{th,1}$ and $v_{dr}/v_{th,2}$ constant. In the reference run, we use the drift velocity and the strength of the magnetic field from Run A. Both the magnetic field and the drift velocities are aligned with the x-axis, mimicking a field-aligned flow that would be inclined with respect to Cartesian coordinate axes in the shock simulations. Ions are not initialized because they have little if any influence on the evolution of EAWs. For the reference run, we set the number of particles per cell per species to $N_{ppc} = 2650$ and the spatial grid resolution to $\lambda_{se} = 40\Delta$. Figures 10, 11, 12, and 13 summarize the behavior of EAWs in the reference PBCS.

Figure 10 depicts the evolution of the electric field in the reference run, revealing predominantly parallel waves with a minor oblique component. The growth rate is $\Gamma_{max}/\omega_{pe} = 0.185$, which closely aligns with the WHAMP prediction of $\Gamma_{max}/\omega_{pe} = 0.2$. Slight variations in the growth rate are observed with changes in the number of particles per cell. Increasing N_{ppc} from 40 to 2650 results in a growth rate variation from 0.14 to 0.185. The peak value over time of the electrostatic field, $\max(|E|/(B_0 c))$ (where $|E|$ is defined as $\sqrt{\langle E^2 \rangle}$ and the average is taken over the simulation box), exhibits only marginal changes within the discussed range of N_{ppc}, increasing from 0.0341 to 0.0359. Notably, the growth rate's influence is not significant, since Equation (4) is always satisfied and EAWs have ample time to reach a nonlinear stage of evolution.

Figure 11 displays the Fourier power spectrum of the electric field parallel to the magnetic field at its maximum intensity ($t\omega_{pe} = 47.5$). The peak of the observed spectrum is in good agreement with the numerically calculated growth rate for the bi-Maxwellian hot-beams dispersion relation. Figure 12 shows the evolution of $k_{max}\lambda_{se}$ (see Equation (3)) in time. At the time of peak power, the wavelength aligns closely with the WHAMP prediction. However, during the nonlinear stage of EAW evolution, $k_{max}\lambda_{se}$ decreases with time approximately by a factor of 2, explaining the discrepancy in wavelength observed in Figure 9. The 2D structure of the EAWs also evolves from coherent waves at $t_1\omega_{pe} = 47.5$ (Figure 13, left panel) to bipolar solitary structures at $t_2\omega_{pe} = 117.5$ (Figure 13, right panel).

PBCSs demonstrate that the growth rate Γ_{max}/ω_{pe} and the maximal electrostatic field strength $\max(|E|/(B_0 c))$ remain independent of the drift velocity, spatial resolution (if waves are properly resolved; e.g., $\lambda_{max} > 10\Delta$), presence or absence of ions, and their mass (assuming $m_i/m_e > 200$). However, the long-term evolution reveals that EAWs decay differently, depending on the drift velocity. Figure 14 shows three PBCS runs with initial conditions drawn from Runs A, C, and E (let us call them PBCS A/C/E). These runs demonstrate different decay behavior at late times ($t > 50\omega_{pe}^{-1}$), where $|E|/(B_0 c)$ is roughly proportional to v_{sh}/c for the chosen time step.

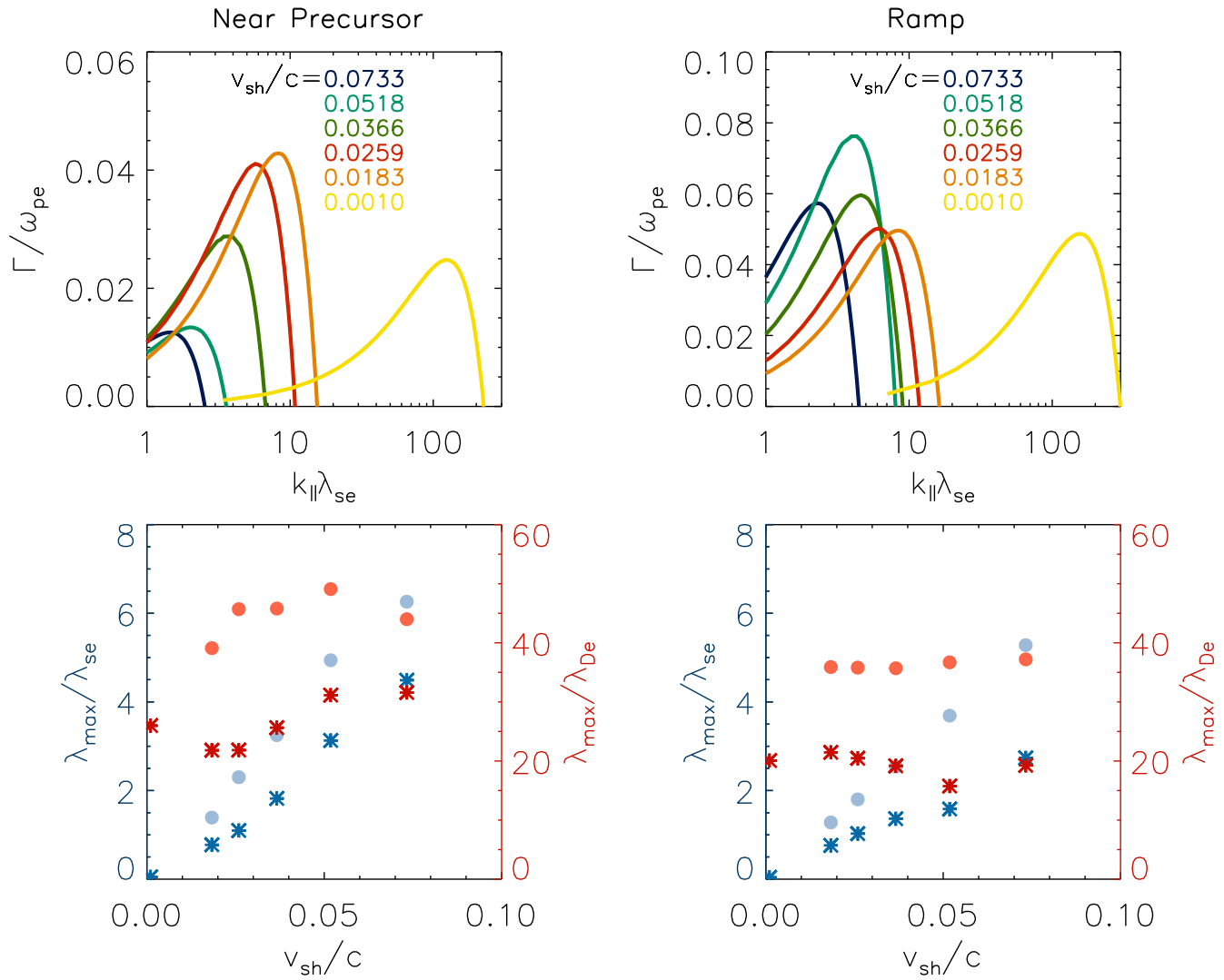

Figure 9. Top panels: the growth rate of the EAWs for the near precursor and shock ramp parameters. Bottom panel: wavelength of the most unstable electron acoustic mode normalized to the electron skin depth (blue asterisks) and the Debye length (red asterisks). The faded red and blue circles show results from the shock simulations (also shown in Figure 7).

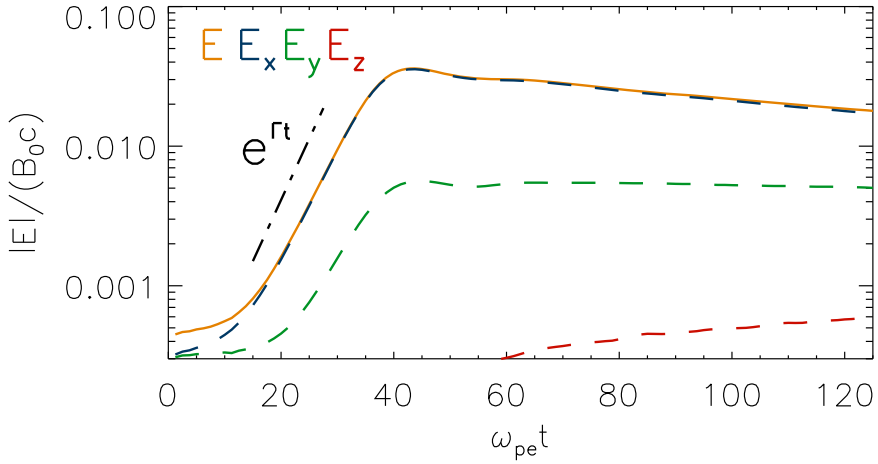

Figure 10. Evolution of rms electric field fluctuation strength, $|E| = \sqrt{\langle E^2 \rangle}$, in the reference PBCS. The dashed–dotted line is the prediction of the linear dispersion analysis, $\Gamma_{max}/\omega_{pe} = 0.2$.

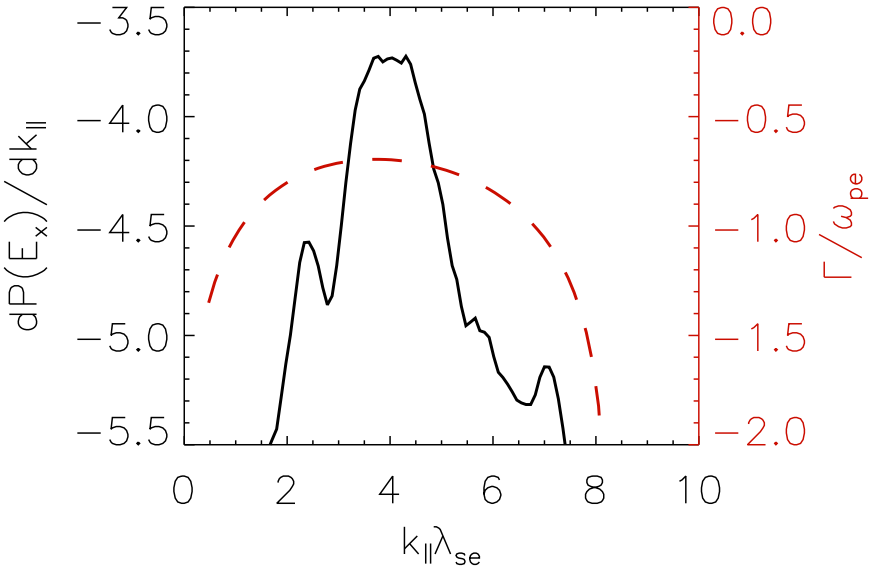

Figure 11. The Fourier power spectrum of the electric field parallel to the magnetic field in the reference PBCS (black solid line) compared with the theoretical prediction (red dashed line).

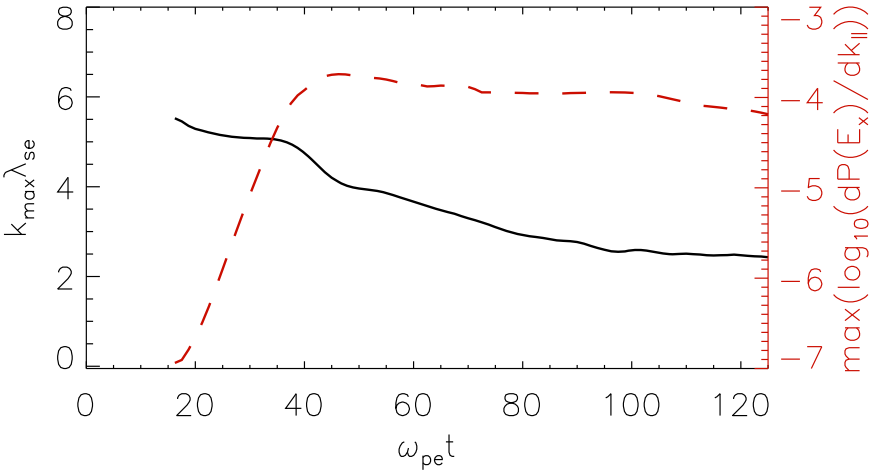

Figure 12. Evolution of the electron acoustic mode k_{max} (black solid line) from its most unstable wavenumber to a lower-k saturated state, and the peak power (red dashed line) in the reference PBCS.

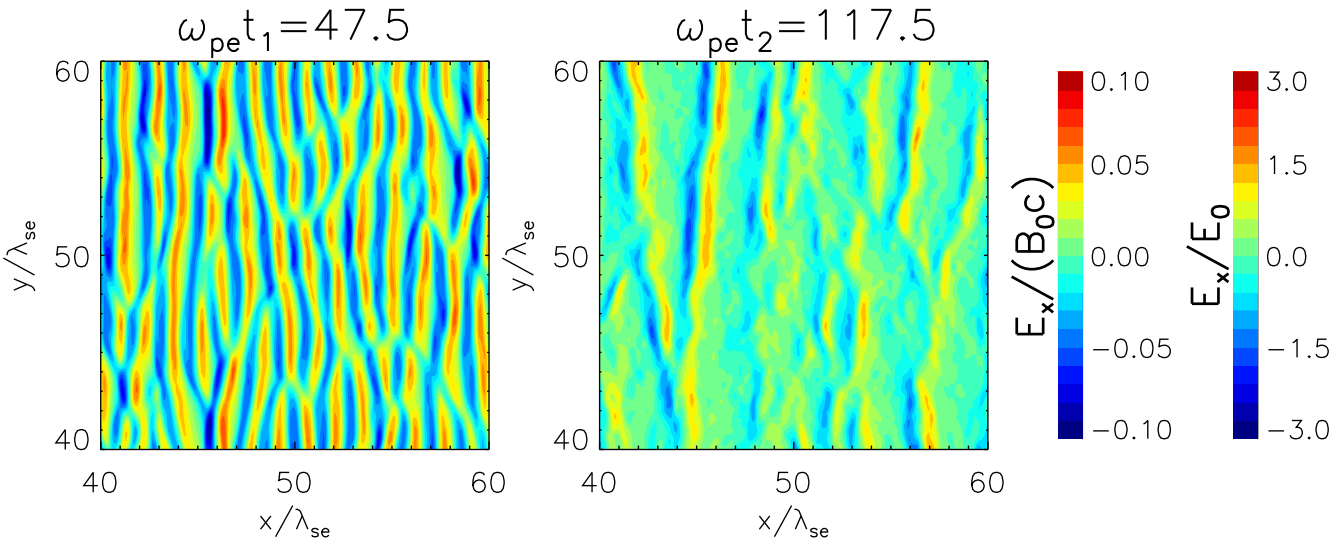

Figure 13. The parallel electric field maps at the maximum power of EAWs (left panel; $\omega_{pe}t_1 = 47.5$) and at the late stage of evolution (right panel; $\omega_{pe}t_2 = 117.5$) in the reference PBCS.

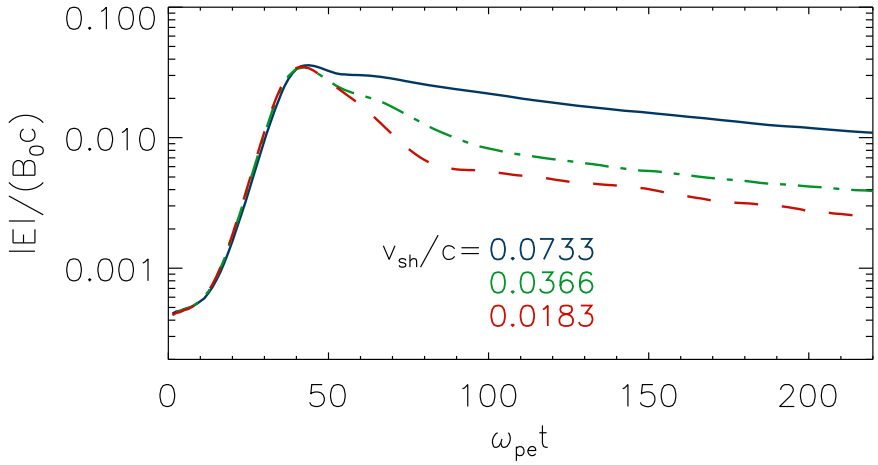

Figure 14. The long-term evolution of the electric field in the reference PBCS and two runs with v_{dr} multiplied by 0.5 and 0.25. These PBCSs mimic shock conditions from Runs A, C, and E.

4. Discussion

The saturated, nonlinear outcome of the electron acoustic instability in the PBCSs agrees with the full-shock simulations in several respects. The decrease of $k_{max}\lambda_{se}$ at late times in Figure 12 can explain why the shock-measured k_{max} differs from the WHAMP linear predictions by approximately a factor of 2 (Table 2, Figure 9). The polarity of the $E_{\parallel}$ structures in the PBCS (Figure 13) matches that of the shock simulations. The PBCSs demonstrate that $\max(|E|/(B_0c))$ does not depend on v_{sh}/c or $(|E|/E_0)^2 \propto (v_{sh}/c)^{-2}$. However, at the end of PBCS A/C/E runs, the electrostatic fluctuation amplitude scales as $|E|/(B_0c) \propto v_{sh}/c$, which implies that $(|E|/E_0)^2$ is constant with respect to v_{sh}/c. Therefore the ESW scaling observed in shock simulations, $\delta E_{\parallel}^2/E_0^2 \propto (v_{sh}/c)^{-1}$, lies in between the scalings obtained for the maximum of electrostatic energy and late-time decay in the PBCSs. Note that $\sqrt{\delta E_{\parallel}^2}$ in the shock simulations and $|E|$ in the PBCSs are almost equivalent, because the EAWs in the PBCSs predominantly generate E_x (see Figure 10), which is parallel to the initial magnetic field, therefore $|E| \approx |E_x| \approx \sqrt{\delta E_{\parallel}^2}$. Nevertheless, we continue using $\sqrt{\delta E_{\parallel}^2}$ when referring to shock simulations and $|E|$ when referring to the PBCS results.

Let us now further discuss some properties of the late-time electrostatic wave power in the PBCS and shock simulations, which we refer to as either ESWs or electron holes.

4.1. ESW Energy Density Scaling with v_{sh}/c

How does the ESW energy density scale with v_{sh}/c (i.e., ω_{pe}/Ω_e) for fixed shock parameters (Mach numbers, plasma beta, and magnetic obliquity)? Let the ESW energy density be some fraction α of the electron beams' drift kinetic energy,

$$\delta E_{\parallel}^2 \sim \alpha m_e n_e v_{dr}^2/2, \tag{5}$$

where α depends on $v_{dr}/v_{th,1}$ and $v_{dr}/v_{th,2}$. If the shock's energy partition into various reservoirs—bulk flows, waves, and particle heating/acceleration—does not vary with v_{sh}/c (all other shock parameters held constant), then the ESW energy density, being one of those reservoirs, should scale as $\delta E_{\parallel}^2/E_0^2 \propto (c/v_{sh})^2$ and $\max(|E|/(B_0c))$ should not depend on the shock velocity. Indeed, we see in the shock simulations (runs B–B1836) that $v_{dr}^2 \sim (m_i/m_e)v_{sh}^2$, therefore the electrons' drift energy $m_e n_e v_{dr}^2/2$ scales linearly with the shock's bulk flow energy $m_i n_i v_{sh}^2/2$ and Equation (5) predicts

$$\delta E_{\parallel}^2/E_0^2 \sim \frac{\alpha m_i n_i v_{sh}^2}{(v_{sh}B_0)^2} \sim \alpha\beta_p M_s^2\left(\frac{c}{v_{sh}}\right)^2. \tag{6}$$

This suggests that $\delta E_{\parallel}^2/E_0^2$ is independent of the mass ratio m_i/m_e for fixed α, which is indeed observed in shock simulations B and B400. Note that v_{sh} is a factor of 2 different for these simulations, so $\delta E_{\parallel}^2/E_0^2$ is expected to be lower by a factor of 4 in B400. In the shock simulations B800 and B1836, however, the decrease of $\delta E_{\parallel}^2/E_0^2$ with higher m_i/m_e is due to worse driving conditions for ESWs: lower $v_{dr}/v_{th,1}$ and $v_{dr}/v_{th,2}$ (see Table 2) lead to lower α and numerical noise. It is important to mention that the worsening of the driving conditions can potentially be caused by the numerical noise itself.

The PBCSs with initial conditions drawn from Runs A–E agree with Equation (6): the same fraction of beam drift kinetic energy is transferred to electrostatic waves regardless of v_{sh}/c during the linear growth stage of the instability and when the electric field fluctuation strength attains its time-series maximum value, $\max(|E|/(B_0c)) \approx 0.03$ (Figure 14). Why do the shock simulations and the late-time PBCS runs (Figure 14) show a different scaling?

First, does the spatial region occupied by the ESWs vary across Runs A–E? In the shock simulations, we measure $\delta E_{\parallel}^2$ averaged over an x-interval of width $\lambda/2$, where λ is the ion-scale precursor wavelength. If the ESWs occupy an x-interval of width $L_x < \lambda/2$, and L_x varies systematically between Runs A–E, then the scaling of $\delta E_{\parallel}^2$ with v_{sh}/c will be biased with respect to Equation (6). As a concrete example, suppose that L_x is the distance that thermal electrons advect during one EAW instability growth time Γ^{-1}, i.e., $L_x \sim v_{sh}/\Gamma$. Further suppose that $\Gamma \sim \omega_{pe}$ and that Γ is independent of v_{sh}/c. Then, $L_x/\lambda_{si} \sim (\omega_{pe}/\Gamma)(m_e/m_i)^{1/2}(v_{sh}/c)$ decreases by a factor of 4 going from Run A to E, so the shock simulation measurements would be interpreted as

$$\left(\frac{\delta E_{\parallel}^2}{E_0^2}\right)_{\text{measured}} = \left(\frac{\delta E_{\parallel}^2}{E_0^2}\right)\frac{L_x}{\lambda/2} \propto \left(\frac{c}{v_{sh}}\right)^1,$$

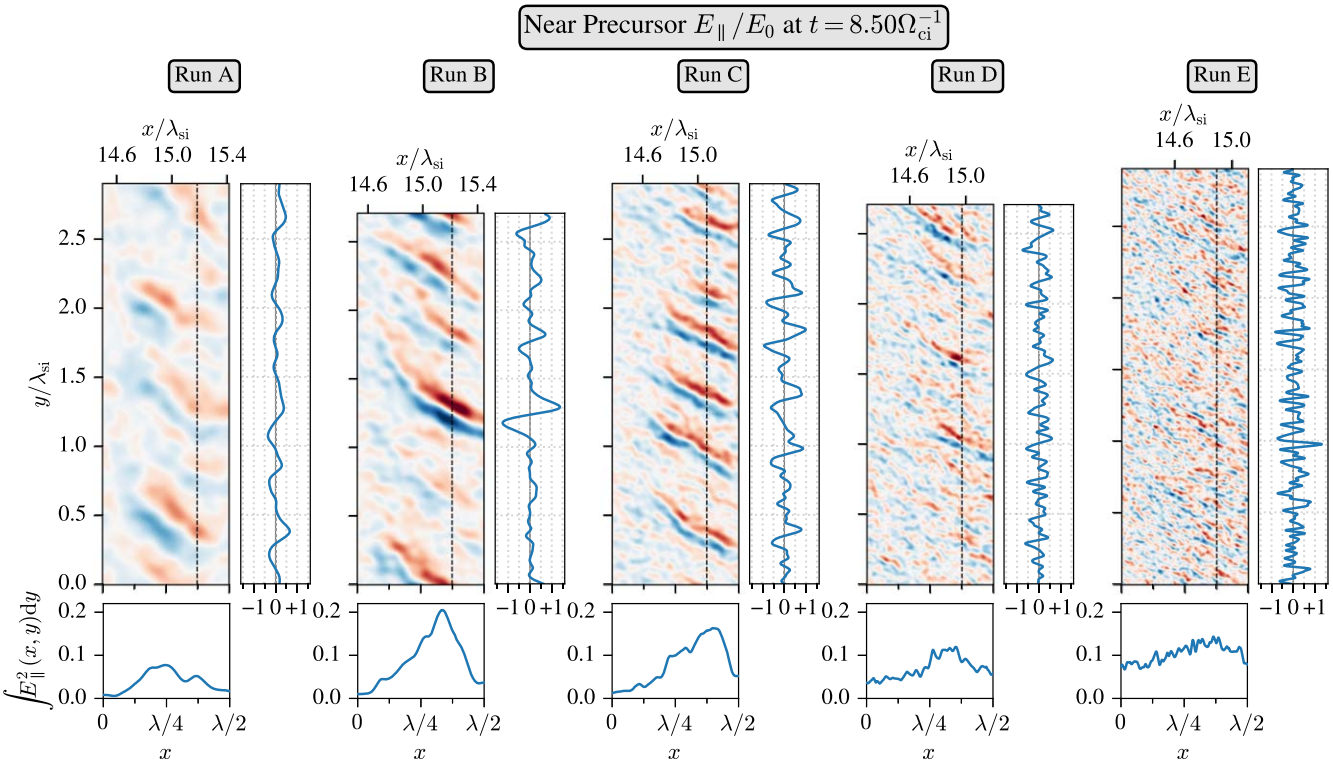

Figure 15. Parallel electric field structure in the "Near Precursor" region for Runs A–E (left to right) at $t = 8.50\Omega_i^{-1}$. Each column of three panels shows one simulation. Within each column, the 2D image shows $E_\parallel/E_0$ with the same color map range as Figure 2 and the horizontal x-axis in units of the ion-scale precursor wavelength λ (the precursor's magnetic minimum is at $x = \lambda/4$). Right of each 2D image, a plot of $E_\parallel(y)$ (blue curve) shows the typical amplitude of ESWs and numerical noise at $x = 3\lambda/8$ (the dashed black line in the 2D image). Below each 2D image, the mean energy density $\int E_\parallel^2(x, y)dy$ is plotted as a function of x (blue curve).

taking $\lambda \approx 2\lambda_{si}$ and assuming $\delta E_\parallel^2/E_0^2 \propto (c/v_{sh})^2$ from Equation (6).

But Figure 15 shows qualitatively that in the "Near Precursor" region, the y-averaged parallel electric field power does not narrow in x-width as v_{sh}/c decreases. The electrostatic waves' spatial width perpendicular to $\boldsymbol{B}$ remains constant, while the wavelength along $\boldsymbol{B}$ shrinks. The variation in L_x thus does not seem to explain our measured $\delta E_\parallel^2/E_0^2$ scaling.

Second, does the saturated ESW amplitude vary between Runs A–E, which would correspond to a change in α in Equation (6)? Following Lotekar et al. (2020, Section 5) and Kamaletdinov et al. (2022, Section IV), an electron hole should saturate in amplitude when an electron's bounce frequency within the hole's electrostatic potential equals either the EAW growth rate Γ or the electron cyclotron frequency Ω_e, i.e.,

$$\omega_{bounce} = \frac{1}{L}\sqrt{\frac{e\phi}{m_e}} \leqslant \min(\Gamma, \Omega_e), \tag{7}$$

where ϕ is the hole's peak electric potential. The case $\omega_{bounce} \sim \Gamma$ is due to nonlinear beam instability saturation; the prefactor in the scaling relation is somewhat uncertain, as discussed by Lotekar et al. (2020). The case $\omega_{bounce} \sim \Omega_e$ is due to hole disruption by transverse instability (Muschietti et al. 2000; Wu et al. 2010; Hutchinson 2017, 2018). These two mechanisms for limiting hole amplitudes predict different scalings of $\delta E_\parallel^2$ with v_{sh}/c. Taking $\phi \sim \delta E_\parallel L$ and $L \sim \lambda_{De}$, Equation (7) may be rewritten:

$$e\delta E_\parallel \lambda_{De} \sim m_e \Gamma^2 \lambda_{De}^2.$$

If ω_{bounce} is bounded by $\Gamma \sim \omega_{pe}$, then we find $\delta E_\parallel^2 \sim 4\pi n_e k_B T_e$, which implies a scaling $\delta E_\parallel^2/E_0^2 \propto (v_{sh}/c)^{-2}$ like Equation (6). On the other hand, if ω_{bounce} is bounded by Ω_e, then $\delta E_\parallel^2 \sim 4\pi n_e k_B T_e (\Omega_e/\omega_{pe})^4$ leads to a different scaling $\delta E_\parallel^2/E_0^2 \propto (v_{sh}/c)^2$.

Taken together, the two mechanisms suggest a nonmonotonic scaling of $\delta E_\parallel^2/E_0^2$ with v_{sh}/c. Recall that lowering v_{sh}/c toward more realistic values is equivalent to raising ω_{pe}/Ω_e, for the fixed shock parameters M_s and β_p. For large v_{sh}/c, as in our PIC simulations, $\Gamma \sim \omega_{pe}$ (up to a constant factor) may be less than Ω_e, such that $\delta E_\parallel^2/E_0^2$ increases as v_{sh}/c falls. Once v_{sh}/c falls enough so that $\Gamma > \Omega_e$ and transverse instability limits the electron hole amplitudes, then $\delta E_\parallel^2/E_0^2$ may peak and then decrease as v_{sh}/c is further lowered.

In our shock simulations, we estimate $\omega_{bounce} \approx 0.076\omega_{pe} = 0.13\Omega_e$ (Run A) and $\omega_{bounce} \approx 0.038\omega_{pe} = 0.27\Omega_e$ (Run E), taking $L = 7\lambda_{De}$ (Section 4.2) and $E_{\parallel,peak}/E_0 = 1$ as typical hole parameters. Both ω_{bounce} estimates lie within the range of $\Gamma_{max} = 0.01$–0.08 for Runs A–E in Table 2, and both estimates are $\gtrsim$4 times smaller than Ω_e. The hole amplitudes thus appear to be limited by Γ and not transverse instability for the range of v_{sh}/c in our simulations.

Electrons in the shock simulations are in steady state. Could transverse instability have been previously excited with $\omega_{bounce} > \Omega_e$, but then stabilized at late times (steady state) to $\omega_{bounce} < \Omega_e$? We evaluate this possibility by inspecting PBCS A/C/E (Figure 14). At high v_{sh}/c (PBCS A), the electron holes are long-lived, whereas as v_{sh}/c decreases, the holes disappear. At $\omega_{pe}t = 40$, when the electric field energy density is greatest,

the hole amplitude $E_x/(B_0c) \approx 0.1$ in all PBCSs (Figures 13 and 14). We then estimate $\omega_{\rm bounce} = 0.50\Omega_e$, $0.97\Omega_e$, and $1.96\Omega_e$ for PBCSs A, C, and E, respectively, which suggests that transverse instability may occur during the nonlinear decay of EAWs into solitary electron holes in PBCSs C and E.

To summarize, in our shock simulations, the scaling of the electrostatic energy density associated with the electron holes, $\delta E_\parallel^2/E_0^2 \propto (v_{\rm sh}/c)^{-1}$, is not well explained by an equipartition argument (Equation (6)). The hole amplitudes must be influenced by the nonlinear saturation of electron flows in a manner that is sensitive to $v_{\rm sh}/c$ (i.e., $\omega_{\rm pe}/\Omega_e$). In matched PBCS simulations, the late-time decay of EAWs into electron holes results in a scaling of $|E|/(B_0c) \propto (v_{\rm sh}/c)^{-1}$ that corresponds to $\delta E_\parallel^2/E_0^2 \propto (v_{\rm sh}/c)^0$, which suggests the importance of a nonlinear phase for electron hole development in shock simulations. The PBCS drives the EAW amplitudes large enough that the EAW decay into electron holes could be mediated by transverse hole instability. We speculate that in shocks, an initial electron-beam-driving process (e.g., during the reflection of a flow off an obstacle) could also form electron holes in such a manner, before settling into the observed steady state.

4.2. Comparison to Observations

Our shock simulations suggest that the driving conditions for ESWs are independent of the shock velocity (Table 2). Therefore, we can expect that these electrostatic waves should be observed in real shocks, even if we use $v_{\rm sh} = 312\,{\rm km\,s^{-1}}$, as in our synthetic Run S. The wavelength $\lambda_{\rm max} = 23\lambda_{\rm De} \approx 200$ m for Run S, averaging the values for the "Ramp" and "Near Precursor" regions and assuming $\lambda_{\rm De} = 8.58$ m at 1 au from the Sun (Wilson et al. 2021). But we need to make two adjustments. First, recall that the holes in our PBCS runs roughly double in wavelength as the simulation proceeds to late times (Figure 12). Second, our $\lambda_{\rm max} = 2\pi/k_{\rm max}$ does not correspond directly to the hole spatial scale L reported in observations (Lotekar et al. 2020; Kamaletdinov et al. 2022). The length L arises from a Gaussian model of a hole's electric potential:

$$\phi(x) = \phi_0 e^{-x^2/(2L^2)}.$$

The Fourier transform of a single hole's $E_\parallel$ signal is

$$\begin{aligned}\tilde{E}_\parallel(k) &= \frac{1}{\sqrt{2\pi}}\int_{-\infty}^{+\infty} e^{-ikx}E_\parallel(x)\,{\rm d}x \\ &= -i\phi_0 Lke^{-k^2L^2/2},\end{aligned} \tag{8}$$

and the power spectrum $|\tilde{E}_\parallel(k)|^2$ has a local maximum at $k = 1/L$. All together, we anticipate $L = 2\lambda_{\rm max}/(2\pi) \approx 7\lambda_{\rm De} \approx 60$ m for our electron holes when scaled to solar wind conditions. This is comparable to the slow electron holes observed at Earth's bow shock—typical size $\sim 5\lambda_{\rm De}$ and range ~ 0.5–$30\lambda_{\rm De}$ (Kamaletdinov et al. 2022)—and also the electron holes seen in Earth's magnetotail (Lotekar et al. 2020).

As previously mentioned, PBCSs of electron beams show that $\max(|E|/(B_0c))$ does not depend on the shock velocity, indicating that $\delta E_\parallel^2/E_0^2$ is proportional to $v_{\rm sh}^{-2}$. However, in shock simulations, it is observed that $\delta E_\parallel^2/E_0^2$ is proportional to $v_{\rm sh}^{-1}$, or $v_{\rm sh}^0$ (Figure 4). By assuming that the true scaling of $\delta E_\parallel^2/E_0^2$ lies between $v_{\rm sh}^{-1}$ and $v_{\rm sh}^{-2}$, and considering that $|\delta E|/E_0$ for individual ESWs reaches 1.64 in Run A, we can estimate that the amplitude of ESWs in a realistic shock scenario should fall within the range of $|\delta E| \approx 1.64\left(\sqrt{\frac{v_{\rm sh,runA}}{v_{\rm sh,runS}}} - \frac{v_{\rm sh,runA}}{v_{\rm sh,runS}}\right) E_0 \approx (14\text{–}116)E_0 \approx (11\text{–}96)\,{\rm mV\,m^{-1}}$. These estimates align well with the values measured by MMS (Wilson et al. 2014a; Goodrich et al. 2018; Wang et al. 2021; Kamaletdinov et al. 2022). In this estimation, we assumed $B_0 = 5.8nT$ (Wilson et al. 2021), resulting in $E_0 \approx 0.83\,{\rm mV\,m^{-1}}$.

Our shock simulations suggest that the electron beams become too hot to drive ESWs as m_i/m_e increases toward the true proton-to-electron value $m_i/m_e = 1836$. The beam drift/thermal velocity ratios $v_{\rm dr}/v_{\rm th,1}$ and $v_{\rm dr}/v_{\rm th,2}$ decrease monotonically with mass ratio m_i/m_e to attain, respectively, 1.2 times and 1.6 times smaller values for Run B1836 as compared to Run B (Table 2). The instability growth rate $\Gamma_{\rm max}/\omega_{\rm pe}$ falls steeply. But our simulations at high m_i/m_e have strong numerical noise, which reduces the distribution anisotropy and hence may bias our estimates of $v_{\rm dr}/v_{{\rm th},e}$ low. And if the electron beams' drift kinetic energy scales linearly with the shock frame's incoming bulk energy $v_{\rm sh}^2$, implying $v_{\rm dr}/v_{{\rm th},e} \propto M_{\rm s}$, a 1 to 2 times increase in $M_{\rm s}$ may suffice to drive EAW-unstable beam drifts in a shock with realistic mass ratio.

In both shock simulations and PBCSs, we observe electron holes with positive polarity (net positive charge and local electric potential maximum). For our chosen shock parameters, few ions reflect at the ramp and the overall shock structure is laminar, so ion–ion streaming does not occur and ion holes of negative polarity (net negative charge and local electric potential minimum) are not generated. In contrast, the bipolar ESWs observed at Earth's bow shock are mostly ion holes. Wang et al. (2021) present a detailed catalog of bipolar ESWs measured in 10 MMS crossings of Earth's bow shock. In eight crossings, electron holes are only 1%–6% of the cataloged bipolar ESWs. However, in the two crossings with lowest $M_{\rm A} = 3.4$ and 4.7, electron holes are ~25% of the cataloged bipolar ESWs. Our simulations are thus most pertinent to lower-Mach crossings of Earth's bow shock and interplanetary shocks in the heliosphere. Further shock simulations encompassing different Mach numbers and obliquities are necessary to investigate the nature of the various ESWs observed near Earth's bow-shock region.

5. Conclusions

In this study, we have identified ESWs observed in low-Mach-number shock simulations as the nonlinear outcome of the electron acoustic instability, which has been confirmed through simulations with periodic boundaries and linear dispersion analysis. These ESWs are driven by two hot counterstreaming electron beams, and the ratio of the drift velocity to the thermal velocity for these beams (in other words, the driving conditions) is independent of the shock velocity. This finding suggests that the same mechanism can be responsible for driving ESWs in shocks with realistic velocities. Additionally, we have observed that the wavelength of ESWs is proportional to the shock velocity, and this expected wavelength under Earth's bow-shock conditions is consistent with in situ measurements obtained by MMS. Furthermore, we have found that the normalized strength of ESWs is roughly inversely proportional to the shock velocity, indicating that in real shocks, their amplitudes would be significantly higher than the quasi-static electric field, aligning

with observations from in situ measurements. However, the usage of the realistic proton-to-electron mass ratio alters the driving conditions and strongly suppresses the occurrence of ESWs for the Mach number and shock obliquity chosen in our study. This suppression is due to a combination of the high electron thermal velocity in comparison to the drift velocity of the two electron beams and significant numerical noise. Better-quality shock simulations are needed to accurately measure the drift/thermal velocity ratio and to suppress numerical noise, in order to assess whether this particular type of ESW may be driven at the true mass ratio. And, in stronger shocks (higher M_s) at $m_i/m_e = 1836$, we also anticipate that higher drift velocities and local (shock-transverse) fluctuations in electron beam driving may drive ESWs.

This study proposes a solution for the discrepancy between PIC simulations and in situ measurements. In PIC simulations, we observe ESWs with parameters (wavelength and amplitude) that differ from those observed at the Earth's bow shock, due to the higher shock velocity used in PIC simulations. However, the nature of the ESWs can be the same as in real shocks. These conclusions can be applied to similar two-stream electrostatic instabilities, such as IAWs, if shocks with different Mach numbers or obliquity are considered. While our focus has been on beams induced by large-amplitude oblique whistlers, this sort of beam–beam interaction and electrostatic wave generation is a generic process. If the driving conditions remain constant across shocks with varying velocities and ion-to-electron mass ratios, the electrostatic waves observed in PIC simulations may appear in real shocks with the correct strength and wavelength. Additionally, it is important to highlight that the small-amplitude and large-wavelength electrostatic waves observed in PIC simulations are a realistic representation of electrostatic waves for the chosen shock velocity, provided that numerical noise is negligible.

Acknowledgments

A.B. was supported by the German Research Foundation (DFG) as part of the Excellence Strategy of the federal and state governments—EXC 2094-390783311. A.T. was supported by NASA FINESST grant No. 80NSSC21K1383 and partly supported by NSF PHY-2010189. L.S. was supported by NASA ATP grant No. 80NSSC20K0565. Some of the work was supported by the Geospace Environment Modeling Focus Group "Particle Heating and Thermalization in Collisionless Shocks in the Magnetospheric Multiscale Mission (MMS) Era" led by L.B.W. III. We acknowledge travel and collaboration support from the ISSI Bern Team "Energy Partition across Collisionless Shocks" (ISSI International Team project #520). We thank Martin Pohl and Ivan Vasko for helpful discussion. The numerical experiments were done with the HLRN supercomputer at the North-German Supercomputing Alliance (projects bbp00033 and bbp00057), the HPC system Raven at the Max Planck Computing and Data Facility (MPCDF), the computer clusters Habanero, Terremoto, and Ginsburg (Columbia University), and Pleiades allocation s2610 (NASA). The latter resources were provided by Columbia University's Shared Research Computing Facility (SRCF) and the NASA High-End Computing Program through the NASA Advanced Supercomputing (NAS) Division at the Ames Research Center. Columbia University's SRCF is supported by NIH Research Facility Improvement grant No. 1G20RR030893-01 and the New York State Empire State Development, Division of Science Technology and Innovation (NYSTAR), Contract C090171.

Data Availability

Public versions of Tristan and WHAMP are available at https://github.com/ntoles/tristan-mp-pitp and https://github.com/irfu/whamp. The scripts required to generate the model data and the figures in this paper are available at doi:10.5281/zenodo.10973653 (Bohdan & Tran 2024).

Appendix
Precursor $E_\parallel$ Power Spectrum in Runs A–E

The Fourier power spectrum of $E_\parallel$ also confirms the propagation direction and speed of the electron holes (Figure 16), serving a similar purpose as Figure 2, but without needing to manually track individual holes. We compute the spectrum for all Runs A–E in the region $x = 10$ to $20\lambda_{si}$ and time interval $t = 8.00$ to $t = 8.50\Omega_i^{-1}$; the measurement is performed in the downstream rest frame (i.e., simulation frame). The time sampling rate $f \approx 0.444\omega_{pe}$ resolves the Langmuir wave power at $\omega \approx \omega_{pe} - k_x v_0$ in the simulation frame, ensuring that it does not alias in frequency space and thereby contaminate the $E_\parallel$ spectral power of interest to us. The Langmuir waves' Doppler shift $k_x v_0$ is $\lesssim 20\%$ of ω_{pe} at $k = 5\lambda_{se}^{-1}$ for all runs, so the waves are unaliased and well separated for the k domain in Figure 16. In all Runs A–E, we observe $E_\parallel$ wave power at $\omega = 0$ to $0.2\omega_{pe}$ that clusters along $\omega = k_\parallel v_{te0}$. The waves occupy a broad bandwidth in both ω and k, which at high k is limited by the damping length scale of the PIC current filtering.

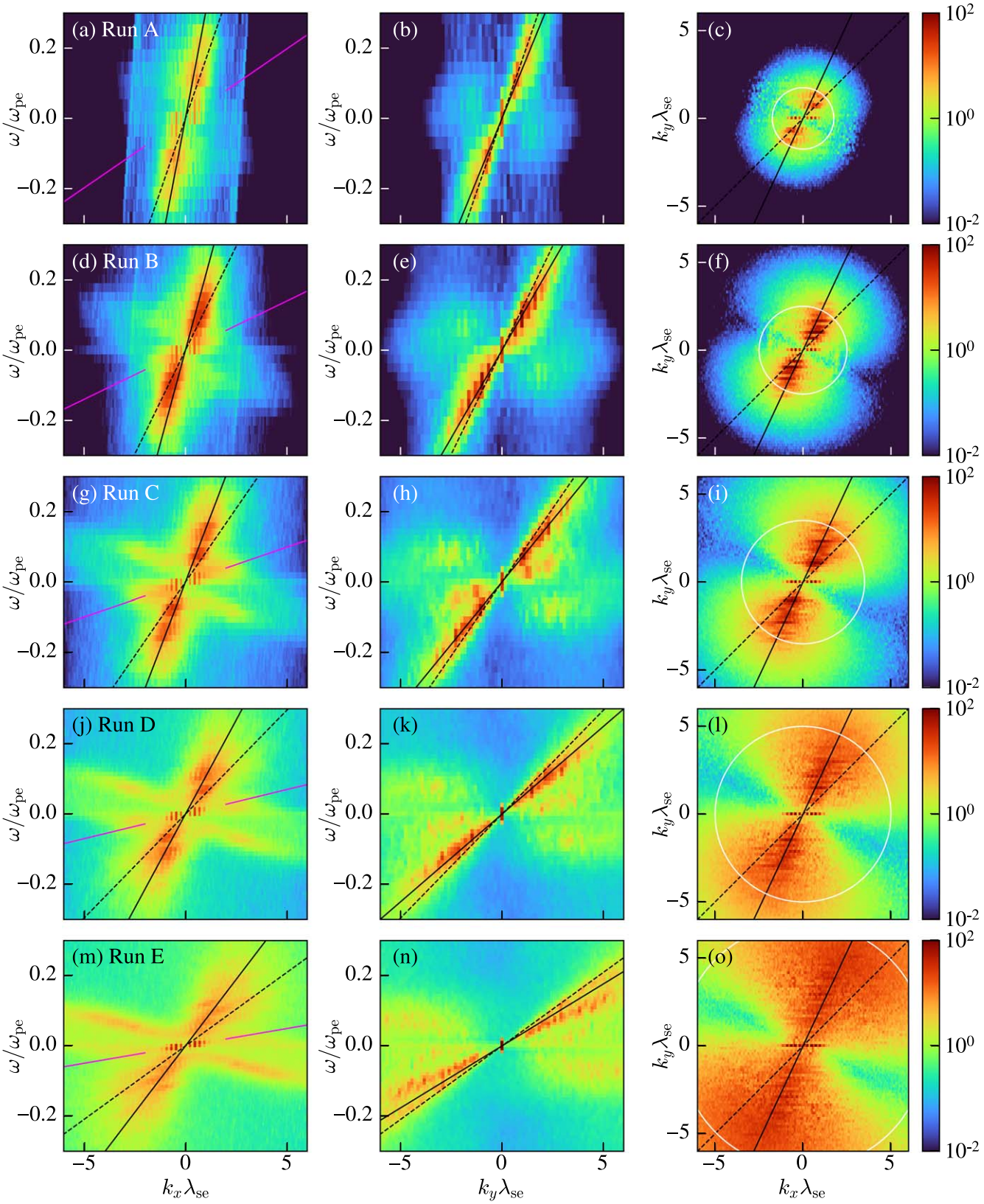

Figure 16. Fourier power spectra of the shock precursor $E_\parallel$ for Runs A–E (top to bottom), measured in the downstream plasma's rest frame. The left column is the (ω, k_x) spectrum; the middle column is the (ω, k_y) spectrum; and the right column is the (k_x, k_y) spectrum. Each column is averaged over all k_y, k_x, and ω, respectively. The low-frequency, phase-standing precursor lies along $\omega/k_x = v_{sh}/r$ (left column, magenta line), where r is the shock's density compression ratio; near the origin, the magenta line is not drawn, so that features of interest can be seen. A broad region of wave power has $\boldsymbol{k}$ along $\boldsymbol{B}$ and a downstream frame phase velocity ω/k that, when boosted to the upstream rest frame, is close to the upstream electron thermal speed v_{te0}. To show this, the solid and dashed black lines plot $\omega = kv_{te0} - k_x v_0$ at propagation angles $\theta = 65°$ and 45°, respectively, measured counterclockwise from $+\hat{\boldsymbol{x}}$ (i.e., $\omega = k_x v_{te0}/\cos\theta - k_x v_0$ (left column) and $\omega = k_y v_{te0}/\sin\theta - k_y v_0/\tan\theta$ (middle column)). The θ angles bracket the range of $\boldsymbol{B}$ orientations within precursor wave troughs. The white circle (right column) is the 50% damping length induced by PIC current filtering (Section 2.1).

ORCID iDs

Artem Bohdan https://orcid.org/0000-0002-5680-0766
Aaron Tran https://orcid.org/0000-0003-3483-4890
Lorenzo Sironi https://orcid.org/0000-0002-1227-2754
Lynn B. Wilson, III https://orcid.org/0000-0002-4313-1970

References

Amano, T., & Hoshino, M. 2007, ApJ, 661, 190
Amano, T., & Hoshino, M. 2009, ApJ, 690, 244
Bale, S. D., Kellogg, P. J., Larsen, D. E., et al. 1998, GeoRL, 25, 2929
Behlke, R., André, M., Bale, S. D., et al. 2004, GeoRL, 31, L16805
Birdsall, C. K., & Langdon, A. B. 1991, Plasma Physics via Computer Simulation (The Adam Hilger Series on Plasma Physics) (Bristol: IOP Publishing Ltd)
Bohdan, A., Niemiec, J., Kobzar, O., & Pohl, M. 2017, ApJ, 847, 71
Bohdan, A., Niemiec, J., Pohl, M., et al. 2019a, ApJ, 878, 5
Bohdan, A., Niemiec, J., Pohl, M., et al. 2019b, ApJ, 885, 10
Bohdan, A., Pohl, M., Niemiec, J., et al. 2020, ApJ, 904, 12
Bohdan, A., Pohl, M., Niemiec, J., et al. 2021, PhRvL, 126, 095101
Bohdan, A., & Tran, A. 2024, Electrostatic Waves and Electron Holes in Simulations of Low-Mach Quasi-Perpendicular Shocks (simulation data and figures) v1, Zenodo, doi:10.5281/zenodo.10973653
Bohdan, A., Weidl, M. S., Morris, P. J., & Pohl, M. 2022, PhPl, 29, 052301
Buneman, O. 1958, PhRvL, 1, 8
Buneman, O. 1993, in Computer Space Plasma Physics: Simulation Techniques and Software, ed. H. Matsumoto & Y. Omura (Tokyo: Terra Scientific), 67
Burch, J. L., Moore, T. E., Torbert, R. B., & Giles, B. L. 2016, SSRv, 199, 5
Burgess, D., Hellinger, P., Gingell, I., & Trávníček, P. M. 2016, JPlPh, 82, 905820401
Chen, L.-J., Wang, S., Wilson, L. B., III., et al. 2018, PhRvL, 120, 225101
Davis, L. A., Cattell, C. A., Wilson, L. B., III., et al. 2021, ApJ, 913, 144
Dieckmann, M. E., Chapman, S. C., McClements, K. G., Dendy, R. O., & Drury, L. O. 2000, A&A, 356, 377
Feldman, W. C., Bame, S. J., Gary, S. P., et al. 1982, PhRvL, 49, 199
Filbert, P. C., & Kellogg, P. J. 1979, JGR, 84, 1369
Forslund, D. W., Morse, R. L., & Nielson, C. W. 1970, PhRvL, 25, 1266
Fredricks, R. W., Coroniti, F. V., Kennel, C. F., & Scarf, F. L. 1970, PhRvL, 24, 994
Fredricks, R. W., Kennel, C. F., Scarf, F. L., Crook, G. M., & Green, I. M. 1968, PhRvL, 21, 1761
Goodrich, K. A., Ergun, R., Schwartz, S. J., et al. 2018, JGRA, 123, 9430
Gurnett, D. A., & Anderson, R. R. 1977, JGR, 82, 632
Horbury, T. S., Cargill, P. J., Lucek, E. A., et al. 2001, AnGeo, 19, 1399
Hoshino, M., & Shimada, N. 2002, ApJ, 572, 880
Hutchinson, I. H. 2017, PhPl, 24, 055601
Hutchinson, I. H. 2018, PhRvL, 120, 205101
Johlander, A., Schwartz, S. J., Vaivads, A., et al. 2016, PhRvL, 117, 165101
Kamaletdinov, S. R., Vasko, I. Y., Wang, R., et al. 2022, PhPl, 29, 092303
Kato, T. N., & Takabe, H. 2010a, ApJ, 721, 828
Kato, T. N., & Takabe, H. 2010b, PhPl, 17, 032114
Kobzar, O., Niemiec, J., Amano, T., et al. 2021, ApJ, 919, 97
Krasnoselskikh, V. V., Lembège, B., Savoini, P., & Lobzin, V. V. 2002, PhPl, 9, 1192
Kurth, W. S., Gurnett, D. A., & Scarf, F. L. 1979, JGR, 84, 3413
Lalti, A., Khotyaintsev, Y. V., Dimmock, A. P., et al. 2022, JGRA, 127, e30454
Lampe, M., Manheimer, W. M., McBride, J. B., et al. 1972, PhFl, 15, 662
Lezhnin, K. V., Fox, W., Schaeffer, D. B., et al. 2021, ApJL, 908, L52
Lotekar, A., Vasko, I. Y., Mozer, F. S., et al. 2020, JGRA, 125, e28066
Lowe, R. E., & Burgess, D. 2003, AnGeo, 21, 671
Malaspina, D. M., Goodrich, K., Livi, R., et al. 2020, GeoRL, 47, e90115
Matsukiyo, S., & Scholer, M. 2006, JGRA, 111, A06104
Melzani, M., Winisdoerffer, C., Walder, R., et al. 2013, A&A, 558, A133
Morris, P. J., Bohdan, A., Weidl, M. S., & Pohl, M. 2022, ApJ, 931, 129
Muschietti, L., & Lembège, B. 2006, AdSpR, 37, 483
Muschietti, L., Roth, I., Carlson, C. W., & Ergun, R. E. 2000, PhRvL, 85, 94
Papadopoulos, K. 1985, in Collisionless Shocks in the Heliosphere: A Tutorial Review (Geophysical Monograph Series) ed. R. G. Stone & B. T. Tsurutani, 34 (Washington, DC: American Geophysical Union), 59
Rönnmark, K. 1982, WHAMP-Waves in homogeneous, anisotropic, multicomponent plasmas v1.4.2, GitHub (https://github.com/irfu/whamp)
Sarkar, S., Paul, S., & Denra, R. 2015, PhPl, 22, 102109
Shimada, N., & Hoshino, M. 2000, ApJL, 543, L67
Sironi, L., & Spitkovsky, A. 2009, ApJ, 698, 1523
Spitkovsky, A. 2005, in Astrophysical Sources of High Energy Particles and Radiation, ed. T. Bulik, B. Rudak, & G. Madejski, Vol. 801 (Melville, New York: American Institute of Physics), 345
Thomsen, M. F., Barr, H. C., Gary, S. P., Feldman, W. C., & Cole, T. E. 1983, JGR, 88, 3035
Tidman, D. A., & Krall, N. A. 1971, Shock waves in collisionless plasmas (Wiley Series in Plasma Physics) (New York: Wiley)
Tran, A., & Sironi, L. 2024, ApJ, 965, 37
Trotta, D., Hietala, H., Horbury, T., et al. 2023, MNRAS, 520, 437
Umeda, T., Yamao, M., & Yamazaki, R. 2009, ApJ, 695, 574
Vasko, I. Y., Mozer, F. S., Bale, S. D., & Artemyev, A. V. 2022, GeoRL, 49, e98640
Verscharen, D., Parashar, T. N., Gary, S. P., & Klein, K. G. 2020, MNRAS, 494, 2905
Walker, S. N., Balikhin, M. A., Alleyne, H. S. C. K., et al. 2008, AnGeo, 26, 699
Wang, R., Vasko, I. Y., Mozer, F. S., et al. 2021, JGRA, 126, e29357
Wilson, L. B., III., Cattell, C., Kellogg, P. J., et al. 2007, PhRvL, 99, 041101
Wilson, L. B., III., Cattell, C. A., Kellogg, P. J., et al. 2010, JGRA, 115, A12104
Wilson, L. B., III, Chen, L.-J., & Roytershteyn, V. 2021, FrASS, 7, 97
Wilson, L. B., III., Sibeck, D. G., Breneman, A. W., et al. 2014a, JGRA, 119, 6475
Wilson, L. B., III, Sibeck, D. G., Breneman, A. W., et al. 2014b, JGRA, 119, 6455
Wilson, L. B., III., Koval, A., Szabo, A., et al. 2012, GeoRL, 39, L08109
Wu, C. S., Winske, D., Zhou, Y. M., et al. 1984, SSRv, 37, 63
Wu, M., Lu, Q., Huang, C., & Wang, S. 2010, JGRA, 115, A10245
Xu, R., Spitkovsky, A., & Caprioli, D. 2020, ApJL, 897, L41
Yu, C., Yang, Z., Gao, X., Lu, Q., & Zheng, J. 2022, ApJ, 930, 155